Community-Driven Code Comparisons for Three-Dimensional Dynamic Modeling of Sequences of Earthquakes and Aseismic Slip (SEAS)

Junle Jiang[1], Brittany A. Erickson[2], Valère R. Lambert[3],

Jean-Paul Ampuero[4], Ryosuke Ando[5], Sylvain D. Barbot[6], Camilla Cattania[7],

Luca Dal Zilio[8,9], Benchun Duan[10], Eric M. Dunham[11], Alice-Agnes Gabriel[12,13],

Nadia Lapusta[8], Duo Li[12], Meng Li[14], Dunyu Liu[15], Yajing Liu[16],

So Ozawa[5], Casper Pranger[9,12], Ylona van Dinther[9,14]

[1]School of Geosciences, University of Oklahoma, Norman, OK, USA

[2]Department of Computer and Information Science, University of Oregon, Eugene, OR, USA

[3]Department of Earth and Planetary Sciences, University of California, Santa Cruz, CA, USA

[4]Université Côte d'Azur, IRD, CNRS, Observatoire de la Côte d'Azur, Géoazur, France

[5]Department of Earth and Planetary Science, University of Tokyo, Japan

[6]Department of Earth Sciences, University of Southern California, Los Angeles, CA, USA

[7]Department of Earth, Atmospheric, and Planetary Sciences, Massachusetts Institute of Technology, Cambridge, MA, USA

[8]Seismological Laboratory and Department of Mechanical and Civil Engineering, California Institute of Technology, Pasadena, CA, USA

[9]Institute of Geophysics, Department of Earth Sciences, ETH Zurich, Zurich, Switzerland

[10]Department of Geology and Geophysics, Texas A&M University, College Station, TX, USA

[11]Department of Geophysics, Stanford University, Stanford, CA, USA

[12]Department of Earth and Environmental Sciences, Ludwig-Maximilians-Universität München, Munich, Germany

[13]Institute of Geophysics and Planetary Physics, Scripps Institution of Oceanography, University of California, San Diego, CA, USA

[14]Department of Earth Sciences, Utrecht University, Utrecht, Netherlands

[15]Institute for Geophysics, University of Texas at Austin, TX, USA

[16]Department of Earth and Planetary Sciences, McGill University, Montréal, QC, Canada

Key Points:

- We pursue community efforts to develop code verification benchmarks for three-dimensional earthquake rupture and crustal faulting problems
- We assess the agreement and discrepancies of seismic and aseismic fault behavior among simulations based on different numerical methods
- Our comparisons lend confidence to numerical codes and reveal sensitivities of model observables to key computational and physical factors

Corresponding author: Junle Jiang, `jiang@ou.edu`

Abstract

Dynamic modeling of sequences of earthquakes and aseismic slip (SEAS) provides a self-consistent, physics-based framework to connect, interpret, and predict diverse geophysical observations across spatial and temporal scales. Amid growing applications of SEAS models, numerical code verification is essential to ensure reliable simulation results but is often infeasible due to the lack of analytical solutions. Here, we develop two benchmarks for three-dimensional (3D) SEAS problems to compare and verify numerical codes based on boundary-element, finite-element, and finite-difference methods, in a community initiative. Our benchmarks consider a planar vertical strike-slip fault obeying a rate- and state-dependent friction law, in a 3D homogeneous, linear elastic whole-space or half-space, where spontaneous earthquakes and slow slip arise due to tectonic-like loading. We use a suite of quasi-dynamic simulations from 10 modeling groups to assess the agreement during all phases of multiple seismic cycles. We found excellent quantitative agreement among simulated outputs for sufficiently large model domains and fine grid spacings. However, discrepancies in rupture fronts of the initial event are influenced by the free surface and various computational factors. The recurrence intervals and nucleation phase of later earthquakes are particularly sensitive to numerical resolution and domain-size-dependent loading. Despite such variability, key properties of individual earthquakes, including rupture style, duration, total slip, peak slip rate, and stress drop, are comparable among even marginally resolved simulations. Our benchmark efforts offer a community-based example to improve numerical simulations and reveal sensitivities of model observables, which are important for advancing SEAS models to better understand earthquake system dynamics.

Plain Language Summary

Fault zone and earthquake processes involve time scales ranging from milliseconds to millennia and longer. Increasingly, computational models are used to simulate sequences of earthquakes and aseismic slip (SEAS). These simulations can be connected to diverse geophysical observations, offering insights into earthquake system dynamics. To improve these simulations, we pursue community efforts to design benchmarks for 3D SEAS problems. We involve earthquake researchers around the globe to compare simulation results using different numerical codes. We identify major factors that contribute to the discrepancies among simulations. For example, the spatial dimension and resolution of the computational model can affect how earthquakes start and grow, as well as how frequently they recur. Code comparisons are more challenging when we consider the Earth's surface in the simulations. Fortunately, we found that several key characteristics of earthquakes are accurately reproduced in simulations, such as the duration, total movement, maximum speed, and stress change on the fault, even when model resolutions are not ideal. These exercises are important for promoting a new generation of advanced models of earthquake processes. Understanding the sensitivity of

⁶⁹ simulation outputs will help test models against real-world observations. Our community efforts
⁷⁰ can serve as a useful example to other geoscience communities.

1 Introduction

⁷²   Physics-based computational models of dynamic processes in the Earth are increasingly used
⁷³ to understand and predict observations from the lab and field across spatial and temporal scales,
⁷⁴ addressing fundamental questions in various branches of solid Earth research. In earthquake science,
⁷⁵ models of earthquake source processes are aimed at capturing dynamic earthquake ruptures from
⁷⁶ seconds to minutes and slow slip processes subject to short-term anthropogenic or environmental
⁷⁷ forcing, or tectonic loading over timescales of years and longer. For individual earthquakes, *dynamic*
⁷⁸ *rupture simulations* have emerged as powerful tools to reveal the influence of fault structure, geometry,
⁷⁹ constitutive laws, and prestress on earthquake rupture propagation and associated ground motion
⁸⁰ (e.g., *Bhat et al.*, 2007; *Day*, 1982; *Duan and Day*, 2008; *Dunham et al.*, 2011a,b; *Gabriel et al.*,
⁸¹ 2012; *Kozdon and Dunham*, 2013; *Lozos et al.*, 2011; *Ma and Elbanna*, 2019; *Nielsen et al.*, 2000;
⁸² *Olsen et al.*, 1997; *Ripperger et al.*, 2007; *Shi and Day*, 2013; *Wollherr et al.*, 2019; *Xu et al.*, 2015).
⁸³ These simulations are limited to single-event scenarios and subject to imposed artificial prestress
⁸⁴ conditions and ad hoc nucleation procedures. For larger-scale fault network systems, a group of
⁸⁵ *earthquake simulators* aims at producing complex spatiotemporal characteristics of seismicity over
⁸⁶ millennial time scales (*Richards-Dinger and Dieterich*, 2012; *Tullis et al.*, 2012). The formidable
⁸⁷ computational demand inevitably requires simplification and approximation of some key physical
⁸⁸ features that could potentially influence or dominate earthquake and fault interactions, such as
⁸⁹ seismic waves, slow slip, and inelastic responses.

⁹⁰   To reveal earthquake system dynamics, it has been widely recognized that we need models
⁹¹ that simulate fault behavior over multiple seismic events and the intervening periods of aseismic
⁹² deformation. To address this need, numerical simulations of Sequences of Earthquakes and Aseismic
⁹³ Slip (SEAS) are developed to consider all phases of earthquake faulting, from slow loading to
⁹⁴ earthquake nucleation, propagation and termination over time scales of milliseconds to millenniums
⁹⁵ in a unified, self-consistent framework (Figure 1). While retaining computational rigor, SEAS
⁹⁶ models capture the pre-, inter-, and post-seismic slip and the resulting stress redistribution that
⁹⁷ ultimately lead to spontaneous earthquake nucleation and dynamic ruptures. SEAS models can also
⁹⁸ incorporate other physical processes relevant to long-term slip such as interseismic healing of the
⁹⁹ fault zone, folding, viscoelasticity, and fluid flow (e.g., *Allison and Dunham*, 2018; *Barbot*, 2018;
¹⁰⁰ *Lambert and Barbot*, 2016; *Sathiakumar et al.*, 2020; *Zhu et al.*, 2020). This modeling framework
¹⁰¹ can help determine and quantify which physical factors control diverse observables such as ground
¹⁰² deformation and shaking, and the frequency, size, and rupture style of microseismicity and large
¹⁰³ earthquakes. SEAS modeling also bridges the domains of dynamic rupture simulations and earthquake

simulators, providing physically justified approximations and self-consistent choices on initial conditions and earthquake nucleation procedures.

Developments in SEAS models over the past two decades have led to increased diversity and complexity of models and closer connections between simulations and observations from the lab and field. For example, seismological and geodetic observations have been combined with models of seismic and aseismic deformation to study fault frictional properties (e.g., *Barbot et al.*, 2009; *Dublanchet et al.*, 2013; *Floyd et al.*, 2016; *Jiang and Fialko*, 2016; *Johnson et al.*, 2006; *Mitsui and Iio*, 2011), aftershock sequences (e.g., *Perfettini and Avouac*, 2004, 2007), tremor and slow slip (e.g., *Dublanchet*, 2018; *Luo et al.*, 2017; *Mele Veedu and Barbot*, 2016; *Tymofyeyeva et al.*, 2019; *Wang and Barbot*, 2020), and characteristics of small and large earthquake ruptures (e.g., *Barbot et al.*, 2012; *Cattania and Segall*, 2019; *Chen and Lapusta*, 2009; *Jiang and Lapusta*, 2016, 2017). The framework of earthquake sequence modeling is also adopted in diverse settings, which include subduction zones (e.g., *Hori et al.*, 2004; *Liu and Rice*, 2005, 2007; *Li and Liu*, 2016, 2017; *Noda et al.*, 2013; *Shi et al.*, 2020; *Van Dinther et al.*, 2013), collision zones (e.g., *Dal Zilio et al.*, 2018; *Michel et al.*, 2017; *Qiu et al.*, 2016), and induced seismicity phenomena (e.g., *Dieterich et al.*, 2015; *McClure and Horne*, 2011), among many applications.

While researchers continue to build more advanced and detailed SEAS models, verification of different numerical codes is essential to ensure credible and reproducible results, and sustain scientific progress. In practice, analytical solutions are generally not available, even for simple SEAS problems, and convergence of simulations to a high-resolution reference case may not always detect systematic issues in complex numerical codes. An alternative means for verifying model results are comparisons of independent numerical codes from different research groups. As an example, the SCEC/USGS Spontaneous Rupture Code Verification Project pioneered the code comparison exercise and improved confidence in the outcomes of dynamic rupture simulations (*Barall and Harris*, 2014; *Harris et al.*, 2009, 2018).

Verification of SEAS models is confronted with distinct challenges, due to the wide range of temporal and spatial scales that characterize the earthquake source behavior and the diversity of numerical algorithms and codes. For example, codes based on spectral boundary element method (SBEM) (*Barbot*, 2021; *Lapusta and Rice*, 2003; *Lapusta and Liu*, 2009) are highly efficient in solving for dynamic earthquake ruptures, albeit with relatively simple fault geometry and bulk. Codes based on boundary element method (BEM) (e.g., *Goswami and Barbot*, 2018; *Kato*, 2016; *Liu*, 2013; *Luo et al.*, 2017; *Nakata et al.*, 2012; *Rice and Tse*, 1986; *Segall and Bradley*, 2012; *Tse and Rice*, 1986) can efficiently simulate earthquake ruptures in problems with more complex fault geometry, often with the approximation of inertia (i.e., "quasi-dynamic" earthquakes). Codes based on the finite difference method (FDM) (e.g., *Allison and Dunham*, 2018; *Erickson and Dunham*, 2014; *Erickson et al.*, 2017; *Mckay et al.*, 2019; *Pranger*, 2020), finite element method (FEM)

140 (e.g., *Liu et al.*, 2020; *Luo et al.*, 2020; *Tal and Hager*, 2018), spectral element method (SEM) (e.g.,

141 *Kaneko et al.*, 2011; *Thakur et al.*, 2020), and hybrid methods (e.g., *Abdelmeguid et al.*, 2019) can

142 flexibly incorporate geometrical and structural complexity in earthquake simulations, usually at a

143 greater computational cost than BEM. For all these codes, common challenges lie in the interaction

144 between the highly nonlinear nature of the SEAS problems and numerical round-off errors, which

145 can lead to the divergence of model behaviors with increasing simulation time. Simulation techniques

146 are further complicated when additional physical factors, e.g., structural complexity, material heterogeneities,

147 and bulk inelastic responses, are incorporated or approximated. However, considering such complexity

148 may be crucial in our efforts to understand earthquakes and predict seismic hazards.

149 We reported our efforts in the SEAS initiative—a working group funded by the Southern

150 California Earthquake Center (SCEC) to perform community code verification exercises for SEAS

151 models—and results from our first two benchmarks, BP1 and BP2, for two-dimensional (2D) SEAS

152 problems in *Erickson et al.* (2020). We gathered 11 independent modeling groups using different

153 numerical codes to participate and compare 2D SEAS simulations. Through code comparisons, we

154 identified how various computational factors, e.g., the model domain size and boundary conditions,

155 influence simulation results in 2D antiplane problems. Our exercises demonstrate an excellent

156 agreement in simulations with a sufficiently large domain size and small grid spacing, lending

157 confidence to the participating numerical codes. We also found that artificial complexity in earthquake

158 patterns can arise due to insufficient numerical resolution for key physical length scales, although

159 ensemble-averaged measures, such as earthquake recurrence times, are more robust than observables

160 from individual simulations, even at poor numerical resolutions.

161 As our community and code capabilities grow, we have made substantial progress to create

162 new benchmarks for three-dimensional (3D) SEAS problems. Here, we present our recent community-driven

163 development of two new 3D benchmarks, BP4 and BP5, and code comparison results for the quasi-dynamic

164 versions of these benchmarks. The dramatically increased computational demand for 3D problems

165 requires us to balance the simplicity and realism of the benchmark problems (Section 2). We examine

166 choices of numerical implementations among the modeling groups to ensure consistent comparisons

167 of a large set of 3D simulations (Section 3). We also design new strategies and metrics for code

168 verification for complex 3D simulations that are often done at the upper limit of numerical resolutions

169 (Section 4). In particular, we explore the sensitivity of diverse model outputs and observables to

170 major computational and physical factors. Through these efforts, we aim to improve and promote a

171 new generation of rigorous, robust numerical codes for SEAS problems, and to potentially inform

172 and interact with other communities that are tackling similar challenges in nonlinear multiscale,

173 multi-physics problems (e.g. *Buiter et al.*, 2016; *Matsui et al.*, 2016; *Maxwell et al.*, 2014; *Nearing*

174 *et al.*, 2018).

2 Community Benchmark Development

2.1 Strategy for Benchmark Design

We follow the principle to start simple and add incremental complexity in the design process of SEAS benchmarks. For 2D benchmark problems (BP1 and BP2), we considered a 1D fault in a 2D antiplane setting to explore how the computational domain size and boundary conditions affect simulation results and how numerical resolution influences earthquake patterns and statistics (*Erickson et al.*, 2020). Overall, we aim to verify different numerical codes through a detailed comparison of simulated fault behavior over multiple time scales. These efforts require a better understanding of the dependence of fault slip history on fault properties, friction laws, initial conditions, model spin-up, and other factors.

Our findings and experience from 2D benchmark exercises prepared us for more complicated 3D benchmark problems. We need to design 3D benchmarks that are tractable for the widest suite of numerical codes and thereby maximize participation of modelers, especially considering the higher computational cost of 3D simulations and distinct capabilities of different codes in the community. For example, codes based on the spectral boundary element method, e.g., BICyclE (*Lapusta and Liu*, 2009), are efficient in solving for quasi-dynamic or fully dynamic earthquake ruptures, but rely on periodic boundary conditions and free surface approximations. Methods based on the finite element method, e.g., EQsimu (*Liu et al.*, 2020), can incorporate more complicated fault geometries and bulk, including a rigorous treatment of the free surface, but may need to balance the domain size with a reasonable computational cost.

Since the participation of many modelers is essential to the success of the code verification exercise, we sought to build a consensus in the community at the very beginning of our benchmark design process. We conducted surveys among the interested modelers to decide on the most preferred benchmark problems. For instance, we have chosen to focus on quasi-dynamic problems for our initial 3D benchmarks, BP4 and BP5, seeing that many numerical codes cannot yet incorporate full inertial effects but adopt the radiation damping approximation (*Rice*, 1993). While we assess a myriad of simulation outputs and develop metrics for model comparisons, we are flexible about the submitted simulation data, given that sometimes substantial code development is needed. During the subsequent development following initial comparisons of benchmark BP4, we learned lessons about the computational cost and have accordingly revised the model parameters and output types for benchmark BP5, hence some minor differences exist between the two benchmarks.

2.2 Benchmark Problem Setup

We developed two benchmarks, BP4 and BP5, for 3D SEAS simulations (Figure 2). Our first 3D benchmark problem, BP4, considers a 3D homogeneous, isotropic, linear elastic whole space

in $\mathbb{R}^3$, defined by $\boldsymbol{x} = (x_1, x_2, x_3) \in (-\infty, \infty)^3$, where x_1, x_2, and x_3 refer to the coordinates in the fault-normal, along-strike, and along-depth directions, respectively. A vertical strike-slip fault is embedded at $x_1 = 0$. We use the notation "+" and "−" to refer to the side of the fault with x_1 positive and negative, respectively. We assume 3D motion, denoting components of the displacement vector $\boldsymbol{u}$ as $u_i = u_i(\boldsymbol{x}, t), i = 1, 2, 3$, in the i-direction. The second 3D benchmark problem, BP5, involves a fault with half the vertical dimension in a 3D half-space, defined by $\boldsymbol{x} = (x_1, x_2, x_3) \in (-\infty, \infty) \times (-\infty, \infty) \times (0, \infty)$, with a free surface at $x_3 = 0$ and x_3 as positive downward. Several model parameters in BP5 are adjusted to allow for reduced computational demand compared with BP4.

Each benchmark problem branches into two versions, depending on the treatment of the inertial effect, i.e., quasi-dynamic (QD) or fully dynamic (FD) earthquake ruptures, which are assigned with different suffixes in benchmark names (e.g., BP4-QD or BP4-FD). Full descriptions of these benchmarks are available online on the SEAS code comparison platform (`https://strike.scec.org/cvws/seas/`) and also included here as supplementary materials. We summarize below the governing equations, constitutive laws, and initial and fault interface conditions that are important for understanding SEAS simulations for both QD and FD problems, and related numerical resolution issues. For better consistency and clarity, we changed a few notations from the original benchmark descriptions.

The 3D fault zone motion is governed by the momentum balance equation, or the equilibrium equation if inertia is neglected:

$$\rho \frac{\partial^2 \boldsymbol{u}}{\partial t^2} = \nabla \cdot \boldsymbol{\sigma} \quad \text{for FD problems;} \tag{1a}$$

$$0 = \nabla \cdot \boldsymbol{\sigma} \quad \text{for QD problems,} \tag{1b}$$

where $\boldsymbol{u}$ is the displacement vector, $\boldsymbol{\sigma}$ is the stress tensor, and ρ is the material density. Hooke's law relates stresses to strains by

$$\sigma_{ij} = K \epsilon_{kk} \delta_{ij} + 2\mu \left(\epsilon_{ij} - \frac{1}{3} \epsilon_{kk} \delta_{ij} \right), \quad i, j = 1, 2, 3, \tag{2}$$

where K and μ are the bulk and shear moduli, respectively. The strain-displacement relations are given by

$$\epsilon_{ij} = \frac{1}{2} \left(\frac{\partial u_i}{\partial x_j} + \frac{\partial u_j}{\partial x_i} \right), \quad i, j = 1, 2, 3. \tag{3}$$

2.2.1 Boundary and Interface Conditions

We have a boundary condition at the surface ($x_3 = 0$) (for only BP5) and an interface condition on the fault ($x_1 = 0$). At the free surface, all components of the traction vector are zeros, namely

$$\sigma_{j3}(x_1, x_2, 0, t) = 0, \quad j = 1, 2, 3. \tag{4}$$

We assume no-opening on the fault, namely

$$u_1(0^+, x_2, x_3, t) = u_1(0^-, x_2, x_3, t), \tag{5}$$

243 and define the slip vector as the jump in horizontal and vertical displacements across the fault:

$$s_j(x_2, x_3, t) = u_j(0^+, x_2, x_3, t) - u_j(0^-, x_2, x_3, t), \quad j = 2, 3, \tag{6}$$

245 with right-lateral motion yielding positive values of s_2. Positive values of s_3 and s_2 occur when the

246 " + " or " − " side of fault moves in the positive or negative x_3 and x_2 directions, respectively.

247 We require that components of the traction vector be equal and opposite across the fault, which

248 yields the following conditions:

$$\sigma_{j1}(0^+, x_2, x_3, t) = \sigma_{j1}(0^-, x_2, x_3, t), \quad j = 1, 2, 3, \tag{7}$$

250 and denote the common values $-\sigma_{11}$, σ_{21}, and σ_{31} by σ (positive in compression), τ_y, and τ_z,

251 respectively, i.e. one normal traction component and two shear traction components. Note that

252 positive values of τ_y indicate stress that drives right-lateral faulting and positive values of τ_z indicates

253 stress that tends to cause the "+" side of the fault to move downward in the positive x_3 direction and

254 the "−" side to move upward.

255 We define the slip rate vector V in terms of its components, $V = (V_2, V_3) = (\dot{s}_2, \dot{s}_3)$, where the

256 dot notation indicates the time derivative, and denote slip rate amplitude as the norm of the slip rate

257 vector, $V = ||V||$. The shear stress vector is given by $\tau = (\tau_y, \tau_z)$.

258 In both benchmark problems, we assign a frictional domain on the fault Ω_f with a finite size

259 of (l_f, W_f), where fault slip is governed by a rate- and state-dependent friction law (*Dieterich*, 1979;

260 *Ruina*, 1983; *Marone*, 1998). The shear stress on the frictional fault τ is set to always equal the

261 frictional strength $F = (F_2, F_3)$, namely

$$\tau = F(\bar{\sigma}_n, V, \theta), \tag{8}$$

263 where $\bar{\sigma}_n$ is the effective normal stress and θ is a state variable.

264 For quasi-dynamic problems (BP4-QD and BP5-QD), $\tau = \tau^0 + \Delta\tau - \eta V$ is the sum of the

265 prestress τ^0, the shear stress change due to quasi-static deformation $\Delta\tau$, and the radiation damping

266 approximation of inertia ηV (*Rice*, 1993), where $\eta = \mu/2c_s$ is half the shear-wave impedance for

267 shear wave speed $c_s = \sqrt{\mu/\rho}$, with the shear modulus μ and density ρ. For fully dynamic problems,

268 $\tau = \tau^0 + \Delta\tau$, where $\Delta\tau$ includes all elastodynamic stress transfers due to prior slip on the fault.

269 The frictional resistance of the fault is the product of the effective normal stress and evolving

270 friction coefficient f on the fault, $\bar{\sigma}_n$, namely

$$F(\bar{\sigma}_n, V, \theta) = \bar{\sigma}_n f(V, \theta) V/V. \tag{9}$$

272 The effective normal stress is taken to be uniform in space and assumed to be time-independent,

273 which is valid due to the symmetry across the fault and the assumption of no fault opening. We

274 adopt a regularized formulation for the rate-and-state friction coefficient (*Lapusta et al.*, 2000)

$$f(V, \theta) = a \sinh^{-1} \left[\frac{V}{2V_0} \exp \left(\frac{f_0 + b \ln(V_0\theta/L)}{a} \right) \right],$$ (10)

276 where L is the characteristic state evolution distance, f_0 is the reference friction coefficient determined

277 at the reference slip rate V_0, and a and b are the parameters for the direct and evolutionary effects,

278 respectively. We couple Eq. 10 with the aging law for the evolution of the state variable (*Dieterich*,

279 1979; *Ruina*, 1983):

$$\frac{d\theta}{dt} = 1 - \frac{V\theta}{L},$$ (11)

281 The spatial distributions of parameters a and b are chosen to create a seismogenic zone with velocity-weakening

282 (VW, $a - b < 0$) frictional properties that is surrounded by areas with velocity-strengthening (VS,

283 $a - b > 0$) frictional properties, with a linear transition zone in-between.

284 Outside the frictional domain Ω_f, we impose a fixed long-term fault slip rate, which we refer

285 to as the plate loading rate V_L, giving rise to the interface conditions:

$$V_2(x_2, x_3, t) = V_L,$$ (12a)

$$V_3(x_2, x_3, t) = 0,$$ (12b)

289 At an infinite distance from the fault ($|x_1| \to \infty$), the far-field displacements should follow:

$$u_2^\pm = \pm \frac{V_L t}{2},$$ (13a)

$$u_1 = u_3 = 0,$$ (13b)

293 where the superscript "±" refers to the "+/–" sides of the fault, associated with positive and negative

294 displacement values, respectively. By imposing this boundary condition, we consider displacements

295 u that are only caused by slip, excluding the deformation that produced the prestress τ^0 in the absence

296 of fault slip. As a result, σ are essentially stress changes associated with the displacement field

297 u relative to the prestress state. We describe an infinitely large model domain in our benchmark

298 problems and leave choices of numerical implementation and approximation to modelers (see section 3.1).

2.2.2 Initial Conditions

300 We choose the initial values of the stress and state on the fault to enable a spatially uniform

301 distribution of initial fault slip rates, given by

$$V = (V_{\text{init}}, V_{\text{tiny}}),$$ (14)

303 where we assign $V_{\text{init}} = V_L$ for simplicity and $V_{\text{tiny}} = 10^{-20}$ m/s to avoid infinity in logarithmic slip

304 rates. To achieve this, we prescribe the initial state over the entire fault with the steady-state value

305 at the slip rate V_{init}, namely

$$\theta(x_2, x_3, 0) = L/V_{\text{init}}.$$ (15)

307 Accordingly, the initial stress vector takes the form $\boldsymbol{\tau}^0 = \tau^0 \boldsymbol{V}/V$, where the scalar pre-stress τ^0 is

308 the steady-state stress:

$$\tau^0 = \bar{\sigma}_{\mathrm{n}} a \sinh^{-1}\left[\frac{V_{\mathrm{init}}}{2V_0} \exp\left(\frac{f_0 + b \ln(V_0/V_{\mathrm{init}})}{a}\right)\right] + \eta V_{\mathrm{init}} \, . \tag{16}$$

311 For quasi-dynamic problems, we need to specify an initial value for slip, which we take to be

312 zero, namely

$$s_j(x_2, x_3, 0) = 0, \quad j = 2, 3. \tag{17}$$

314 For fully dynamic problems, initial values for displacements and velocities in the medium need

315 to be specified. We spare the details here since our code comparisons below will be limited to

316 quasi-dynamic problems BP4-QD and BP5-QD.

317 To break the lateral symmetry of the fault and facilitate code comparisons, we add a square

318 zone within the VW region, with a width of $w = 12\,\mathrm{km}$ and centers at $(-22.5\,\mathrm{km}, -7.5\,\mathrm{km})$ in BP4

319 and $(-24\,\mathrm{km}, -10\,\mathrm{km})$ in BP5, as a forced nucleation location for the first simulated earthquake. To

320 do that, we impose a higher initial slip rate, V_{i}, in the x_2 direction within this square zone while

321 keeping the initial state variable $\theta(x_2, x_3, 0)$ unchanged. The resultant higher pre-stress can be

322 calculated by replacing V_{init} with V_{i} in Eq. 16. This initial condition leads to an immediate initiation

323 of the first event. In BP5, we additionally use a smaller characteristic state evolution distance L

324 in this forced nucleation zone to promote the nucleation of subsequent earthquakes in the same

325 areas (see the next section). We note that it will be interesting for future benchmarks to use a ramp

326 function instead of a step function for the nucleation zone to unify spatial discretization of the

327 nucleation zone (*Galis et al.*, 2015).

328 In simulations, the governing equations (1)–(3) are solved along with interface conditions (4)

329 (for only BP5) and (5)–(13), and initial conditions (14)–(17) over the period $0 \leqslant t \leqslant t_{\mathrm{f}}$, where t_{f} is

330 the maximum simulation time. Numerical methods that truncate model domain in the fault-normal

331 direction also need to explicitly incorporate the far-field boundary conditions on asymptotic behavior

332 of displacements at infinity (see section 3.1). All model parameters in benchmarks BP4-QD and

333 BP5-QD are listed and compared in Table 1.

2.2.3 Critical Physical Length Scales

335 Numerical resolution is a critical issue for 3D benchmark problems, as we need to balance the

336 computational cost and adequate resolution to achieve acceptable model agreement. Two physical

337 length scales are generally important to consider in these problems. The first length scale, often

338 referred to as the process zone or cohesive zone, Λ, describes the spatial region near the rupture

339 front under which breakdown of fault resistance occurs, and shrinks as ruptures propagate faster

340 (*Freund*, 1998; *Palmer and Rice*, 1973; *Day et al.*, 2005). For faults governed by the rate-and-state

friction, the quasi-static process zone at a rupture speed of 0^+, Λ_0, can be estimated as follows (*Ampuero and Rubin*, 2008; *Perfettini and Ampuero*, 2008):

$$\Lambda_0 = C \frac{\mu L}{b \sigma_{\rm n}}, \tag{18}$$

where C is a constant of order 1.

The second length scale that controls model behavior is the critical nucleation zone size h^*, which determines the minimum dimension of the velocity-weakening region over which spontaneous nucleation may occur (*Ampuero and Rubin*, 2008; *Andrews*, 1976a,b; *Day*, 1982; *Rubin and Ampuero*, 2005). For 3D problems, the critical nucleation size can be estimated for the aging law for $0.5 < a/b < 1$ as follows (*Chen and Lapusta*, 2009):

$$h^* = \frac{\pi}{2} \frac{\mu b L}{(b-a)^2 \sigma_{\rm n}}. \tag{19}$$

Using Eqs. 18 and 19, we estimate that the nucleation zone size is 12.4 km and 12.5 km within the VW region (outside the zone of frictional heterogeneity) in BP4 and BP5, respectively, whereas the process zone is 2 and 6 km, respectively. This allows us to suggest a grid spacing of 500 m and 1000 m for low-order accurate methods for BP4 and BP5, respectively, which resolve Λ_0 with at least four grid points in both benchmarks, following suggestions by *Day et al.* (2005).

The two benchmark problems are designed to produce a periodic sequence of spontaneous earthquakes and slow slip, following the first event in which we impose higher local slip rates to kickstart the earthquake rupture. BP5 is slightly different from BP4 in that the state evolution distance is reduced within a square zone within the VW region, resulting in a smaller nucleation size, $h^* = 11.6$ km. This form of persistent frictional heterogeneity is introduced to favor (but not always determine) the initiation of subsequent earthquakes at the same location. We choose the total simulation time to produce up to eight large earthquakes in the simulations, which allows us to examine not only a few early events but also the seismic behavior of the fault in the longer term.

2.3 Model Outputs

To assess model behavior over disparate spatial and temporal scales, we design several types of simulation outputs for these benchmarks (Figure 3): (1) time series of local on-fault and off-fault properties, (2) time series of global source properties, (3) a catalog of earthquake characteristics, (4) profiles of slip accumulation and stress evolution, and (5) rupture times during the first event in the sequence. The output formats for coseismic observables follow the practice in the code verification of single-event dynamic rupture simulations (*Harris et al.*, 2009).

For local time series data, we are mostly interested in resolving the time evolution of fault slip rates, shear stress, and off-fault displacements throughout the coseismic, postseismic, and interseismic periods. The "global" source properties refer to the evolving maximum slip rates and

moment rates over the entire seismogenic fault areas, which are useful for determining the precise time of initiation and cessation of individual earthquakes. The catalog data contain key characteristics of simulated earthquakes, including their initiation and termination times, coseismic slip, and stress drop. The beginning and end of the coseismic period are determined as the moments any point on the fault reaches above or all points drop below a threshold slip rate, V_{th} (chosen as 0.03 m/s), respectively. We then estimate coseismic slip and stress drop as the change in the amplitude of fault slip and shear stress (negative stress change for positive stress drop).

The slip and stress profiles in the along-strike and along-dip directions illustrate the general patterns of earthquake sequences and the partitioning of seismic and aseismic slip. The rupture time data record the time when each point on the fault reaches a certain threshold slip rate (V_{th} = 0.03 m/s) during the first earthquake. Note that the relative rupture times are independent of V_{th} and we can use maximum slip rates and rupture time data to construct contours of rupture fronts associated with different values of V_{th}.

2.4 Modeling Groups

To maximize participation, we focus on the quasi-dynamic version of the 3D benchmarks and anticipate new comparisons in future as the computational capabilities of the community grow. A total of 10 modeling groups participated in the code comparisons for the quasi-dynamic problems, BP4-QD and BP5-QD, using nine different numerical codes. We summarize numerical codes and methods, modeling groups, and their participation in either or both benchmarks in Table 2. Note that the simulations hosted on our online platform are named after the username of the modeler who uploaded the data; we include the names here for reference.

We discussed preliminary code comparison results for 3D benchmarks in two workshops in January and October of 2020. We also used the opportunities to share scientific progress and decide on the directions of our future efforts, with substantial inputs from students and early career scientists. Our online platform (https://strike.scec.org/cvws/seas/) facilitates the initial comparison of benchmark results, where modelers can upload and immediately visualize time series data and rupture front contours to assess model agreements.

More modeling groups participated in BP5-QD than BP4-QD, due to considerations of timing and/or computational costs (Table 2). Given the similar problem setup of the two benchmarks, we present main results for BP4-QD and more complete comparisons for BP5-QD, using a selected suite of simulations listed in Tables 3 and 4. Due to limitations in code development and computational resources or different numerical methods, not all modeling groups have submitted all forms of requested simulation outputs. Our comparisons use the entire set of available simulation results.

3 Computational Factors

Both 3D SEAS benchmarks are computationally challenging: BP4-QD requires better numerical resolution and BP5-QD incorporates additional effects associated with the free surface. The overall high computational cost means that we have to carefully consider the effects of computational domain truncation and grid discretization on simulations that are performed near the marginal numerical resolutions. We elaborate on these computational factors in this section to provide important context to our code comparison results. We also comment on the time stepping schemes, an important ingredient in SEAS simulations.

3.1 Domain Truncation and Boundary Conditions

In the benchmark descriptions, we prescribe a whole space or semi-infinite half-space. All numerical codes need to truncate the computational domain in certain dimensions and adopt boundary conditions. While comprehensive tests about the effect of computational domain truncation and boundary conditions were conducted for our 2D benchmark problems (*Erickson et al.*, 2020), they are less feasible for 3D SEAS simulations due to the much higher computational demand. We therefore let modelers determine sufficiently or reasonably large domain sizes using the suggested (or sometimes larger) grid spacing, with the aim of obtaining well-matching results. We denote the total model dimension in the fault-normal, along-strike, and along-dip directions as L_1, L_2, and L_3, respectively, and list the domain size of all simulations in Tables 3 and 4.

In general, BEM/SBEM simulations only discretize the fault interface and solve for on-fault physical properties, implicitly incorporating bulk response via semi-analytical solutions. This feature avoids the need of domain truncation in the fault-normal direction; hence in Tables 3 and 4 we denote ∞ as the fault-normal dimension in BEM/SBEM simulations. Along lateral directions, BEM simulations with FDRA include three large elements outside the friction-controlled domain to construct semi-infinite loading zones of a dimension of 10^4 km. BEM simulations with ESAM, HBI, TriBIE, and Unicyle adopt same- or similar-sized elements and incorporate deep creep in the semi-infinite domain via a commonly used "backslip" approach, in which stress transfers are calculated for spatially-varying fault slip rates subtracted with V_L. Hence the down-dip dimensions in these simulations are effectively infinite, even though we list the actual dimension of the adopted computational domain in Tables 3 and 4.

BEM/SBEM simulations with ESAM, BICyclE, and Motorcycle adopt periodic boundaries that effectively involve infinite replicas of the model domain in the along-strike direction; large areas with the imposed loading rate were included to minimize the effect of adjacent fault replicas on simulated fault behavior. Simulations with BICyclE also have periodic boundary conditions in the along-depth direction and, in the half-space problem BP5, approximate the free surface by

441   adding a mirror image of the physical domain. Nonetheless, in our comparisons we do not observe

442   systematic differences between BICyclE and other simulations that suggest the influence of this

443   approximation.

444   For volume-discretized methods such as EQsimu and GARNET, modelers need to truncate

445   model domains in all three dimensions. For the far-field boundaries in the fault-normal direction,

446   EQsimu and GARNET simulations use a Dirichlet boundary conditions for displacements via a

447   fixed slip rate. When truncated fault-normal dimensions are not sufficiently large, the results will

448   be quantitatively influenced by this boundary condition. In BP5-QD, EQsimu modelers chose the

449   steady interseismic velocity predicted by $V(x_1) = V_{\mathrm{L}}/\pi \cdot \arctan(x_1/H)$ (*Savage and Burford*, 1973),

450   specifically, $V \approx 4 \times 10^{-10}$ m/s (with $H = 18$ km and $x_1 = L_1/2 = 50$ km), to impose displacement

451   boundary conditions in the far field. Both EQsimu and GARNET impose stress-free conditions at

452   the remaining boundaries of the truncated domain, which includes two planes perpendicular to the

453   fault and the bottom layer.

454   With computational resources as the only limiting factor, these different approaches are in

455   principle compatible with the boundary conditions at infinity as outlined in our benchmark descriptions.

456   In our code comparison exercises, we will consider the effects of domain truncation and boundary

457   conditions, especially for marginally resolved simulations.

3.2 Grid Discretization

459   The two benchmarks, especially BP5-QD, have a relatively large grid spacing by design, which

460   is a nontrivial factor when we compare different simulations. For example, different codes represent

461   local fault properties within piece-wise constant (BEM) or piece-wise linear (FEM) elements, or

462   on Fourier sample points (SBEM). In the former case, most BEM codes use rectangular elements,

463   whereas TriBIE uses triangular elements with their centroids on irregular grids. Additionally, FDM

464   code GARNET uses a staggered grid, which means that slip rates are not located on the same grid

465   points with some other properties. Consequently, the representing grid points in these simulations

466   are often offset from the observational points specified in the benchmark description. Even though

467   these numerical codes are designed to solve the same continuum problem, different discrete representations

468   of local physical properties, when combined with a large grid spacing, result in nontrivial truncation

469   errors that are different among these codes.

470   During early code comparisons for BP5-QD, we noticed that a spatial offset in the computational

471   grid can lead to noticeable differences in the location and size of the forced nucleation region and

472   rupture front development during the first event. Even though we have improved the consistency in

473   model setups through several iterations among modelers, the inherent differences in computational

474   methods will contribute to model discrepancies. While this issue does not substantially affect our

2D benchmark problems (*Erickson et al.*, 2020), it appears important in the comparisons for our 3D benchmarks, likely due to the use of larger cells.

3.3 Time Stepping Schemes

The schemes for non-uniform, adaptive time stepping are essential in SEAS simulations that resolve various stages of the seismic cycle. We do not cover this computational aspect in the benchmark description, and presume that modelers will adopt the optimal time stepping schemes for their numerical codes. Most codes use adaptive Runge-Kutta methods for time stepping. FDM code GARNET uses a linear multistep method (BDF2, second order backward differentiation formula) for their time stepping (*Pranger*, 2020). SBEM code BICyclE determines the adaptive time steps based on maximum slip rates and stability conditions derived from constitutive laws (*Lapusta et al.*, 2000), which has also been adopted in other codes, such as EQsimu and GARNET.

In practice, suboptimal time stepping can complicate model comparisons. In earlier comparisons for BP4-QD, one BICyclE simulation (`jiang`) exhibited frequent aseismic transients prior to large events, while these features were absent in another BICyclE simulation (`lambert`). We later tracked down the cause of this discrepancy: the latter simulation adopts a smaller constant factor in estimating the time step size (Eq. 18 in *Lapusta et al.* (2000)) and the use of finer time steps apparently eliminates the aseismic transients, which are numerical artifacts. We encountered a similar situation with EQsimu simulations, where a simple refinement of all time steps could remove numerical transients and improved model agreement. Since we have fixed this issue in updated models, the choice on time stepping approaches should have a minimal influence on the comparison results presented below.

4 Comparisons of 3D Simulations

We examine a range of simulation outputs in the two benchmarks to understand model sensitivities and verify different numerical codes. We first show the agreement and self-convergence of models in BP4-QD (Figures 4–6), followed by more complete comparisons for BP5-QD (Figures 4 and 7–17). These comparisons include the rupture fronts of the first earthquake in the sequence (Figures 4 and 7), the long-term fault behavior in terms of maximum slip rates and earthquake characteristics (Figures 5 and 9), cumulative slip profiles (Figures 6 and 8), on-fault local stress and slip rate evolution in the long term (Figures 10 and 11) and during the coseismic period (Figure 12 and 14), as well as off-fault displacement behavior (Figure 15). Furthermore, we explore the relationship between interseismic stressing history and earthquake recurrence intervals (Figure 16) and the resolvability of coseismic observables in simulations with different spatial resolutions (Figure 17).

4.1 Whole-Space Problem BP4-QD

4.1.1 Initial Rupture Propagation

The initial stage of the simulations provides a few crucial observables that are minimally affected by cumulating numerical errors. For benchmark BP4-QD, we first compare the coseismic rupture fronts during the first event in simulations with the suggested grid spacing ($\Delta x = 500$ m) (Figure 4a). We adopt a higher threshold slip rate than specified in the benchmarks, $V_{th} = 0.1$ m/s, to define the initiation time of the earthquake as the moment when any point on the fault reaches V_{th}; we will later explore how a different V_{th} affects BP5-QD comparisons in section 4.2.1. In Figure 4a, we find an excellent match of rupture fronts in the simulations, with a discrepancy of less than 1 s in local rupture time. The first simulated earthquake initiates within the forced nucleation zone and propagates outward through the rest of the VW region over a period of $\sim$30 s. The suite of simulations with a grid spacing of 1000 m includes two volume-discretized codes. While the discrepancy in rupture times increases to a few seconds among all codes, the qualitative rupture pattern is unchanged in the coarser-resolution simulations.

4.1.2 Long-term Fault Behavior

We then assess the long-term fault behavior, in terms of maximum slip rates over the seismogenic fault areas, in simulations with different resolutions (Figure 5). The simulations with a 1000 m grid spacing come from a wider range of codes and show similar features of earthquake recurrence and interseismic periods, with fault slip rates varying between $\sim 10^{-9}$ and 1 m/s. Since the spatial model resolution is suboptimal, the simulations show a large variability in the transient aseismic slip between large earthquakes. These transient features are completely absent in simulations with a 500 m grid spacing and hence are numerical artifacts, rather than physical features. We also notice a persistent discrepancy of large event recurrence intervals even among better resolved simulations.

The computational demand of 3D benchmark problems prohibits a comprehensive self-convergence test of all participating numerical codes. We use the SBEM simulations (`lambert`) to demonstrate that self-convergence of simulation results may not show the true solution of the mathematically defined benchmark problems, when the domain size is not sufficiently large. In Figure 6, we show simulations with a range of grid spacings (125, 250, 500, and 1000 m) and three computational domain sizes: (120 km, 90 km), (240 km, 180 km), and (480 km, 360 km) for the along-strike and along-dip model dimensions, denoted as S1, S2, and S3, respectively.

The comparison of these simulations using the same code suggests some challenges in assessing model agreement in 3D problems. First, with a smaller computational domain size (S1), simulations appear to converge to a similar pattern of long-term behavior (Figure 6a–b). However, when the computational domain size is increased (S2 and S3), the simulations produce different earthquake

541   patterns, with alternating nucleation locations (Figure 6c–d). This difference results in a minor,

542   though noticeable, change in the recurrence time of subsequent events. The sensitivity of nucleation

543   location in BP4-QD likely results from the spatially uniform frictional properties and near-symmetric

544   stress field associated with the fault-spanning quasi-dynamic earthquake ruptures. Even though we

545   are approaching the computational limit, we expect that model behavior will presumably stabilize

546   and converge to the same pattern as domain size substantially increases, as we have seen in 2D

547   problems (*Erickson et al.*, 2020).

4.2 Half-Space Problem BP5-QD

4.2.1 Initial Rupture Propagation

550   The rupture fronts of the first event in BP5-QD simulations show an excellent agreement with

551   each other, with slightly increased discrepancy compared with BP4-QD results (Figure 4). The

552   simulated earthquake rupture propagates into the transition zones around the VW region and reaches

553   the surface, with the total rupture lasting over 30 s. The maximum discrepancy in local rupture

554   time is less than two seconds among most simulations, and a few seconds between the EQsimu

555   simulation and others, with the former showing higher rupture speeds.

556   When we use a lower threshold slip rate, $V_{th} = 0.03$ m/s, to determine the coseismic phase, the

557   rupture front contours appear more discrepant, though retaining a qualitative agreement among

558   simulations (Figure 7a). This alternative comparison reveals a large variability in the evolution

559   of slower slip preceding the earthquake rupture among simulations. Increased discrepancies are

560   found among SBEM/BEM simulations, while the largest discrepancies are associated with the two

561   volume-discretized codes, which seem to produce rupture speeds that are either higher or lower

562   than the average values among the group. Nonetheless, a smaller grid spacing helps reduce the

563   differences in rupture fronts between EQsimu and other simulations, albeit at an increased computational

564   expense (Figure 7b).

4.2.2 Long-Term Fault Behavior

566   We first show the overall earthquake patterns in BP5-QD (Figure 8). We juxtapose the profiles

567   of fault slip partitioning in the along-strike and along-depth directions from two codes, FDRA and

568   BICyclE, based on BEM and SBEM methods, respectively. The results show that, following the

569   first earthquake, later events exhibit recurrent slip patterns. The coseismic slip occurs within the

570   VW region and into the shallow VS region, whereas postseismic and interseismic slip occurs in the

571   adjacent VS regions and to a lesser extent near the surface. In contrast to BP4-QD, these BP5-QD

572   simulations have a persistent location for earthquake initiation due to the heterogeneity in frictional

573   properties that we introduced in this benchmark.

574   We found overall good agreements of maximum slip rates over the seismogenic fault areas

575   among simulations with the suggested resolutions ($\Delta x = 1000$ m) (Figure 9a). The inter-event times

576   of simulated earthquakes vary around ~235 years over the 1800-year simulation period. A small

577   yet persistent difference in recurrence intervals can lead to apparent divergent timing of large events

578   in simulations, especially for the EQsimu simulation, which appears to be affected by some pre-event

579   aseismic transients. Despite the minor discrepancy in rupture fronts shown earlier, the total rupture

580   duration and stress drop of the first event match closely among simulations for which catalog data

581   are available (Figure 9b-c). We determine the beginning and end of the coseismic period as the

582   moment any point on the fault reaches above or all points drop below a threshold slip rate of 0.1

583   m/s, respectively, to be consistent with how we estimate the rupture time in Figure 4. The simulated

584   earthquakes have robust characteristics, with rupture durations of ~30 s and stress drops of ~5

585   MPa.

586   We then examine the time evolution of local slip rates and shear stress on the fault, at the

587   surface ($x_3 = 0$ km) and the mid-seismogenic depth ($x_3 = 10$ km), during the first 1000 years of

588   BP5-QD simulations (Figures 10 and 11). The periodic variations in local shear stress and slip

589   rates are distinct at different depths. At the surface, large coseismic strength drops are accompanied

590   with small stress drops due to the VS properties of the near-surface layer (Figure 10). In contrast,

591   substantial coseismic stress drops occur within the VW region during earthquakes followed by

592   interseismic strain buildup, leading to slip rate variations over tens of orders of magnitude (Figure 11).

593   We observe a slightly larger discrepancy between simulations at depth than at the surface. Despite

594   noticeable differences in earthquake recurrence times, all simulations accurately capture the full

595   range of slip rate and stress variations. While simulations performed at the suggested resolution

596   ($\Delta x = 1000$ m) already show good agreements in terms of the long-term fault behavior, a smaller

597   grid spacing ($\Delta x = 500$ m) further improves the results.

4.2.3 Coseismic Rupture and Off-Fault Behavior

599   The comparisons of individual earthquake ruptures reveal high consistency among different

600   simulations, as well as some complexity in the development and location of earthquake nucleation

601   processes. In Figure 12, we show the time evolution of shear stress and slip rate at three representative

602   locations: within the forced nucleation zone ($x_2 = -24$ km, $x_3 = 10$ km), at the surface ($x_2 = x_3 = 0$ km),

603   and within the rupture propagation zone ($x_2 = 0$ km, $x_3 = 10$ km) during the first event in the sequence.

604   All time series data are aligned relative to the earthquake initiation time (defined with a threshold

605   slip rate $V_{th} = 0.1$ m/s) in each simulation. Consistent with Figure 4, all simulations show a good

606   agreement in coseismic slip rate and stress evolution, with some minor differences in peak slip

607   rates.

608   For the simulated fourth event, we found slightly increased model discrepancies, due to subtle

609   differences in the earthquake nucleation condition resulting from the prior slip history (Figure 13).

610   While most simulations retain the same source evolution function, the results from two simulations

611   with TriBIE and EQsimu appear qualitatively different over much of the seismogenic zone. This

612   pronounced difference is due to the different initiation locations of the earthquake. Since the nucleation

613   zone in BP5-QD has a large size, the majority of the deeper VW zone hosts aseismic slip. These

614   areas can serve as alternative locations to start an earthquake, when the local stress conditions

615   below the central VW zone outcompete the favorable nucleation zone in our benchmark design.

616   When we compare simulations with a halved grid spacing of 500 m, the variability of nucleation

617   location in TriBIE and EQsimu simulations disappears. The distinct behavior of these simulations

618   based on BEM and FEM methods suggests that the earthquake nucleation in this benchmark is still

619   susceptible to the specific setup of a computational model.

620   To further assess model convergence, we compare the sixth event in simulations with smaller

621   grid spacings of 500 and 250 m (Figure 14). Simulations with a grid spacing of 500 m show excellent

622   agreements. However, we notice emergent complexity in BICyclE simulations that indicates a

623   different nucleation location of the sixth event. Similar to the aforementioned results about TriBIE

624   and EQsimu, we find that earthquake nucleation in finer-resolution simulations (250 m) with BICyclE

625   return to the same location that matches other simulations. In spite of such variability in a few

626   simulations, the clear improvements in model agreement suggest that different numerical codes

627   will likely converge to well-resolved physical behavior with a decrease in the grid spacing.

628   We also compare the off-fault behavior of simulation groups where these outputs are available

629   (Figure 15). Note that most simulations explicitly solve for off-fault responses, except for the case

630   of BICyclE (`lambert`), where off-fault displacements are calculated using previously simulated

631   fault slip history and semi-analytical Green's functions (*Okada*, 1992). For codes Unicycle and

632   TriBIE, off-fault displacements are calculated in the simulations using Okada Green's functions for

633   only fault patches in the frictional domain, excluding deep-seated displacement. For a consistent

634   comparison with other simulations, we add long-term displacement trend to off-fault time series

635   from Unicycle and TriBIE simulations using $V(x_1) = V_L/\pi \cdot \arctan(x_1/H)$ (*Savage and Burford*,

636   1973), where $H = 18$ km.

637   Focusing on the first and fourth event, we observe a good qualitative agreement of surface

638   velocity time series at various distances away from the fault, with the later (fourth) event more

639   challenging to match (Figure 15a–b). Overall, the discrepancies in coseismic slip rate evolution

640   appear larger than all the on-fault properties that we examined. This is likely due to multiple factors,

641   including inaccurate representations of surface observation points (grid points offset from the surface)

642   and domain truncation in the fault-normal direction. The long-term displacement history at these

643   off-fault locations also yield good qualitative agreements (Figure 15c).

4.2.4 Model Discrepancy and Convergence

From previous comparisons, we observe that long-term model observables such as recurrence intervals appear more variable than short-term earthquake characteristics such as coseismic slip and stress drop. To better understand the long-term divergence of simulation results, we explore the interseismic stressing history and its relationship with earthquake recurrence intervals (Figure 16). We first calculate the changes in shear stress within the seismogenic zone in the postseismic and interseismic period leading up to the sixth event. The mid-seismogenic stressing history features higher positive stressing in the early postseismic period due to decaying afterslip, followed by increasing positive stressing in the later interseismic period and negative stressing as the creep fronts enter the seismogenic zone. We can estimate the minimum stressing rate (in insets of Figure 16a and c) when the postseismic period transitions to the interseismic period. This minimum stressing rate is well-defined and less susceptible to the complex fault slip history, hence reflecting differences in large-scale, long-term loading in each simulation.

In both simulation groups using grid spacings of 1000 and 500 m, we found that the minimum interseismic stressing rate is approximately inversely correlated with the nearly constant recurrence intervals of large events (Figure 16b and d). This minimum stressing rates in volume-discretized codes EQsimu and GARNET tend to deviate from the cluster of SBEM/BEM results, although the general relationship between interseismic stressing rates and recurrence intervals still holds. The subsequent stressing history appear more variable among many simulations, especially in cases with a grid spacing of 500 m, indicating the complexity in aseismic slip evolution. These comparisons suggest that stress buildup process is essentially similar across simulations and explain why these simulations have more robust earthquake characteristics, even in the presence of growing discrepancies in the long term.

We then characterize the convergence of these simulations with different resolutions, in terms of three observables of simulated earthquakes (Figure 17). We plot the total rupture duration, and final slip and peak slip rate at the center of the VW region ($x_2 = 0\,\text{km}$; $x_3 = 10\,\text{km}$) during the first and sixth events, because these quantities capture the overall or local properties of earthquake ruptures. We have included BEM/SBEM simulations with resolutions from 2000 m down to 250 m, and FEM/FDM simulations with a smallest grid spacing of 500 or 1000 m. We found a better agreement in these observables for the first event than the sixth event and a closer match in simulations with smaller grid spacings, consistent with our earlier results (Figures 4, 12, and 14). As the convergence test of simulations are not always computationally feasible for these 3D problems, these comparisons provide an alternative approach to verify the involved numerical codes.

5 Discussions

5.1 Important Computational and Physical Factors

The choice of computational domain size has a major influence on simulation results, often in concert with other computational factors such as grid spacing and boundary conditions. The comparisons of global fault properties in BP4-QD (Figures 5 and 6) demonstrate that simulations with a specific code (BICyclE) can robustly produce certain earthquake patterns and characteristics with a decreasing grid spacing. However, the apparent self-converging behaviors are associated with specific domain sizes. The differences between these cases imply that the adopted domain sizes are not sufficiently large to solve the semi-infinite domain problem. The model discrepancy persists due to the variability of earthquake nucleation locations, even when we adequately resolve the cohesive zone during rupture propagation with a grid spacing of 125, 250 and 500 m. These results for BP4-QD suggest that domain truncation prevents simulations from converging toward the solution to the semi-infinite domain problem, at least with current computational resources.

Improvements in benchmark design can at least mitigate some complicating factors. In BP5-QD, we introduced persistent frictional heterogeneity to promote earthquake initiation at the same locations, thereby largely eliminating a key contributor to model discrepancies. The excellent agreement among simulated earthquake properties (Figure 17) further suggest that some model observables are less sensitive to computational factors such as the domain size.

The rupture front contours are diagnostic of rupture behavior and hence a key metric for model agreement, as noted for single-event dynamic rupture simulations (*Barall and Harris*, 2014; *Harris et al.*, 2009). In SEAS simulations, we found various factors that lead to large discrepancies in rupture fronts even during the first event. Some factors are fixable issues, such as inaccurate or inconsistent model setup and parameter choices (Section 3). Some factors can be mitigated in improved benchmark design. For example, when revising BP5-QD, we increased the elevated initial slip rate, V_i, in the forced nucleation zone from 0.01 m/s to 0.03 m/s. This change shortens the period of pre-rupture stress buildup that turn out to be sensitive to the domain size, and improves agreement of the first earthquake.

Other issues represent inherent challenges in resolving the physical problem, e.g., when the free surface is involved. The comparison between BP4-QD and BP5-QD simulations with a grid spacing of 500 m (Figures 4a and 7b) suggests that the presence of the free surface and its interaction with earthquake rupture contribute to increased model discrepancies, even though the cohesive zone is better resolved in BP5-QD. Since we do not have simulations for the exact BP5-QD model setup in both whole space and half-space, we cannot directly characterize the effect of the free surface on 3D benchmark results.

5.2 From 2D to 3D Benchmarks

The experience and findings from our code verification exercises for 2D SEAS benchmarks (*Erickson et al.*, 2020) are indispensable for code comparisons of 3D SEAS models. Strict self-convergence tests are often feasible in 2D problems, allowing us to comprehensively explore how suboptimal choices of computational domain size and model resolution can affect earthquake recurrence intervals and event statistics. The findings from 2D benchmarks hence serve as essential reference examples when we grapple with the effects of various computational factors in challenging 3D problems.

Benchmark problems in 3D have several unique features. First, the complexities of benchmark problems and consideration of computational constraints motivate the design of verification methods and metrics that reveal the relative sensitivities of different model observables. Specifically, earthquake rupture characteristics such as rupture duration, final slip, and peak slip rate appear to be more robust than other longer-term observables such as recurrence intervals and nucleation phase, because domain-size-dependent loading can substantially affect the timing of aseismic slip evolution. Additionally, global fault properties are more robust than local fault behavior, as expected. Second, the 3D nature of the problem brings new physical complexity, in particular the multiple potential locations for earthquake nucleation, compared with the single downdip nucleation location in 2D antiplane problem (*Erickson et al.*, 2020). The interactions of stress heterogeneity and frictional properties throughout the fault slip history ultimately control earthquake nucleation, which cannot be chosen *a priori* by modelers. Third, the 3D setting and the presence of a free surface enables a direct comparison of model results and more complicated geophysical observations, which is important for the efforts to potentially validate SEAS models.

We highlight a few important outcomes of our code comparison results in connections to our 2D exercises. First, excellent quantitative agreements in key model observables can be achieved with proper numerical resolution among different modeling group. Second, at marginal resolutions, several factors combine to affect model agreements and convergence. For this reason, we find generally larger discrepancies among the earthquake ruptures of 3D SEAS simulations than those in 2D SEAS and 3D single-event dynamic rupture simulations. Third, even in well-resolved models, long-term model observables are more sensitive than earthquake observables to minor differences in computational factors.

5.3 Implications for Model Validation

Our successful code comparison exercises lend confidence to the accuracy of the participating numerical codes, serving as an essential step towards the goal of creating valid, physics-based models for earthquake source processes. In our benchmarks, many simulated physical quantities can be measured or inferred with geological and geophysical methods covering distinct temporal

745 and/or spatial scales, such as seismograms, Global Navigation Satellite System (GNSS), satellite

746 imagery, and paleoseismic records, offering opportunities to compare SEAS models with diverse

747 observations. Furthermore, our efforts to understand how sensitive and variable model observables

748 are to both computational and physical factors also contribute to quantifying and reducing uncertainty

749 in the data-model integration. Ultimately, SEAS models validated with real-world observations and

750 through testable predictions can contribute to evaluating the hazard scenarios of past and potential

751 future earthquakes.

752 Despite computational challenges, the SEAS modeling framework presented here rigorously

753 resolves the important temporal and spatial scales in earthquake source processes, in ways that are

754 complimentary to and synergistic with dynamic rupture simulations and earthquake simulators. On

755 the one hand, the computational rigor and realistic physical processes in SEAS modeling can help

756 inform and improve the choices of procedures and parameterization, and approximation of physics

757 in other modeling frameworks. Examples include the design of self-consistent pre-rupture stress

758 conditions, and assessing the role of transient slow slip in time-dependent hazard. On the other

759 hand, the capabilities of other modeling approaches to connect with additional observations can

760 also improve the design of and help validate SEAS models.

6 Conclusions

762 We present code comparison results for 3D models of earthquake sequences and aseismic

763 slip from two recent benchmarks in the SEAS initiative (*Erickson et al.*, 2020). The increased

764 complexity and computational cost of 3D SEAS problems motivate us to adopt new strategies

765 for benchmark design and code verification using a range of simulation outputs. We assess the

766 contours of coseismic rupture fronts, time series of fault slip, slip rates, and shear stress, time series

767 of off-fault displacement and velocity, and history of maximum fault slip rates, as well as earthquake

768 catalogs, from tens of simulations contributed by 10 modeling groups.

769 We achieve excellent model agreements among most outputs and observables with relatively

770 large computational domain size, although discrepancies are slightly larger than those in 3D single-event

771 dynamic rupture and 2D SEAS simulations, partly due to spatial resolutions limited by the computational

772 cost. The successful code verification exercises lend confidence to the accuracy of participating

773 numerical codes. The quantitative differences of simulation results depend on computational factors

774 such as model domain size, grid discretization and spacing, and boundary conditions. Coseismic

775 observables appear more robust than longer-term, aseismic observables that are more easily influenced

776 by domain-size-dependent loading. Understanding the causes of model discrepancies and relative

777 sensitivities of various model observables are important, as researchers work towards integrating

778 the outputs of numerical simulations with the increasing volumes of geological and geophysical

779 observations.

The earthquake problem is a prime example of a dynamic solid-Earth system that span wide-ranging time and space scales. Our community-driven code verification efforts are aimed at improving and promoting a new generation of rigorous, robust numerical codes for earthquake science. Our results and lessons could be useful to other research areas that involve numerical simulations of nonlinear, multi-scale dynamic problems.

Open Research

Our online platform (https://strike.scec.org/cvws/seas/) hosts the simulation data for local and global fault properties and rupture times. The descriptions of benchmarks BP4 and BP5 are available at https://strike.scec.org/cvws/seas/download/ (SEAS_BP4_QD.pdf and SEAS_BP5.pdf) and included as supplementary materials. See the references in Table 2 for the availability of numerical codes. Code GARNET is available at https://bitbucket.org/cpranger/garnet.

Figure 1. Main ingredients and observables in 3D models of sequences of earthquakes and aseismic slip (SEAS).

(a) In a conceptual model of a strike-slip fault zone subject to long-term tectonic plate loading, microseismicity and large earthquakes (hypocenters denoted by red stars) initiate at depths, and large events propagate (rupture front contours in red) through the seismogenic layer (gray), whereas aseismic motion occurs in deeper and sometimes shallower regions (yellow). (b) The space and time scales associated with diverse fault zone processes that can be reproduced in 3D SEAS models. The observables of these processes include interseismic strain accumulation, slow slip, fault creep, dynamic ruptures of microseismicity and large earthquakes, and associated ground shaking and deformation.
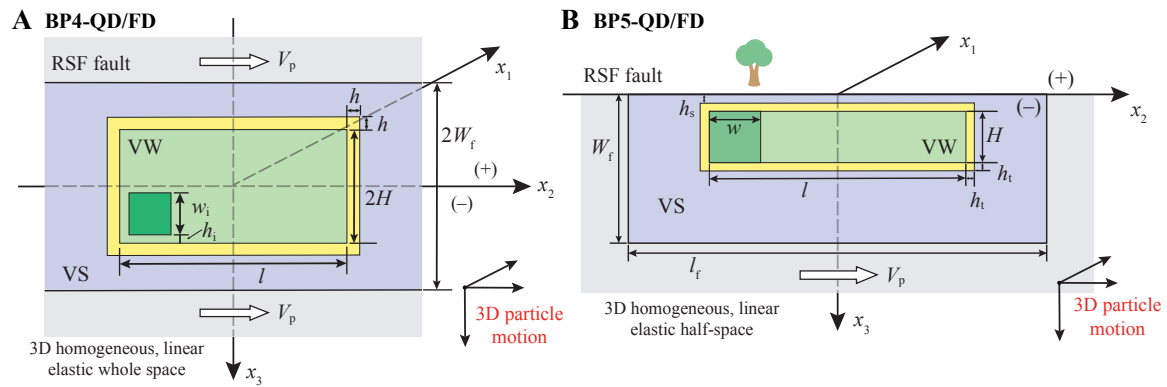
Figure 2. Two benchmark problems for 3D SEAS models. The benchmarks (a) BP4 and (b) BP5 consider 3D motion with a vertical planar fault embedded in a homogeneous, isotropic, linear elastic whole space and a half-space with a free surface, respectively. The fault is governed by a rate-and-state friction (RSF) law in the central region (non-gray colors) with a size of $(\infty, 2W_f)$ for PB4 and (l_f, W_f) for BP5, and creeps at an imposed constant plate loading rate at the boundaries (gray). The velocity-weakening region (light and dark green), with a size of $(l, 2H)$ for BP4 and (l, H) for BP5, is surrounded by a transition zone (yellow) and velocity-strengthening regions (blue). The initial nucleation zone (dark green square) is located at one end of the velocity-weakening region. Earthquakes spontaneously nucleate and propagate across the seismogenic fault.
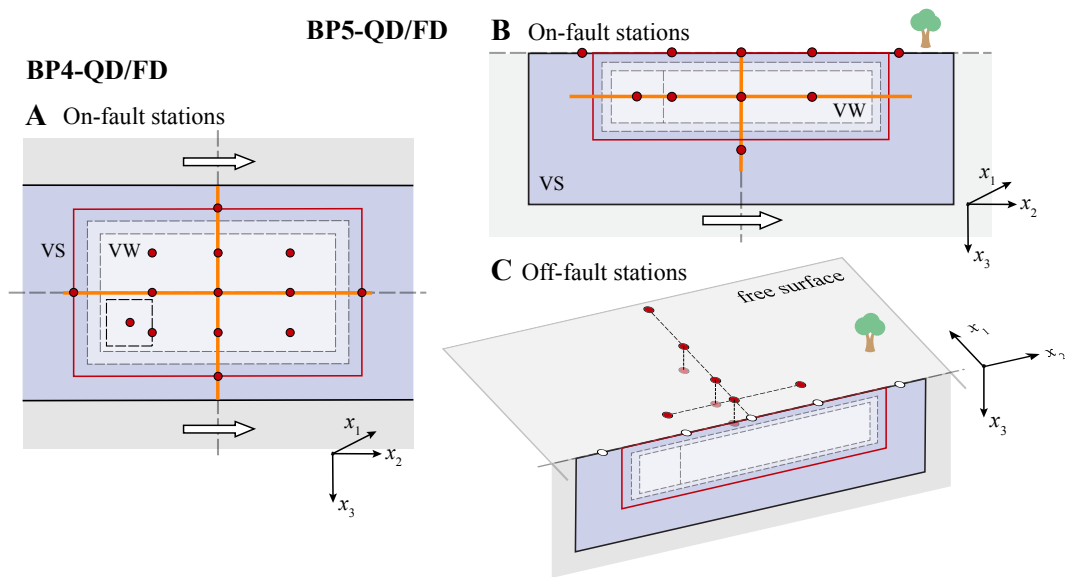
Figure 3. Simulation outputs for 3D SEAS benchmarks. Observation points, lines, and areas are shown for (a) BP4 and (b and c) BP5. Local time series is produced at (a and b) on-fault and (c) off-fault points (red). Slip and stress evolution profiles are produced along cross-section lines (orange). The region outlined in red is considered in estimating time-dependent source properties and rupture front contours. Dashed rectangles indicate fault areas with different frictional properties.
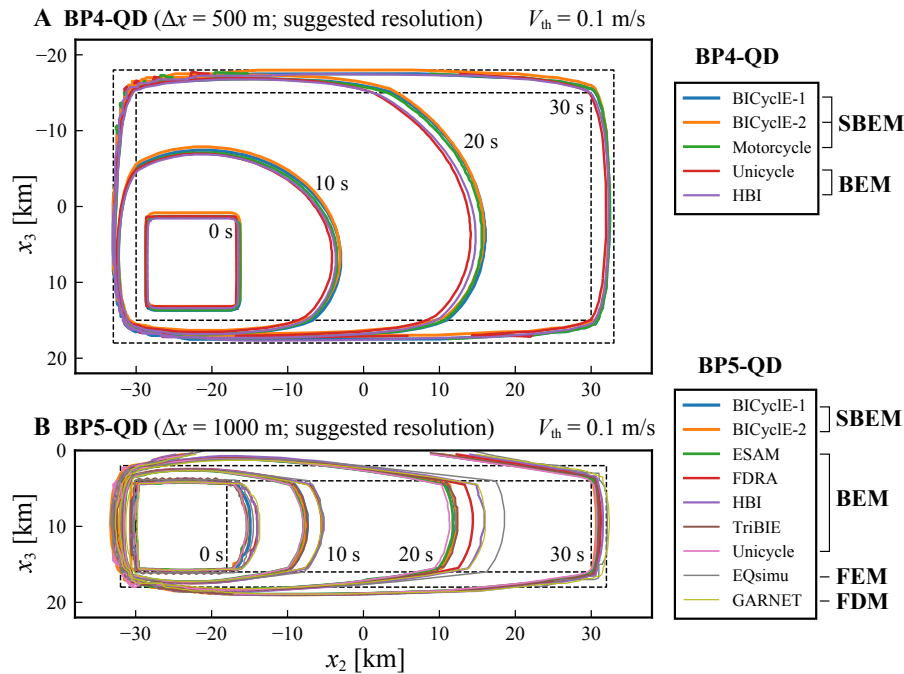
Figure 4. Rupture fronts of the first earthquake in BP4-QD and BP5-QD simulations with suggested numerical resolutions. The contours of rupture fronts are shown for simulations in (a) BP4-QD ($\Delta x = 500$ m) and (b) BP5-QD ($\Delta x = 1000$ m). The rupture front contours indicate 0, 10, 20, and 30 s after the earthquake initiation time, defined as the moment any point on the fault reaches a threshold slip rate $V_{th} = 0.1$ m/s. The legends show code names and corresponding types of numerical methods listed in Table 2. BICyclE-1 and BICyclE-2 refer to simulations from `jiang` and `lambert`, respectively.
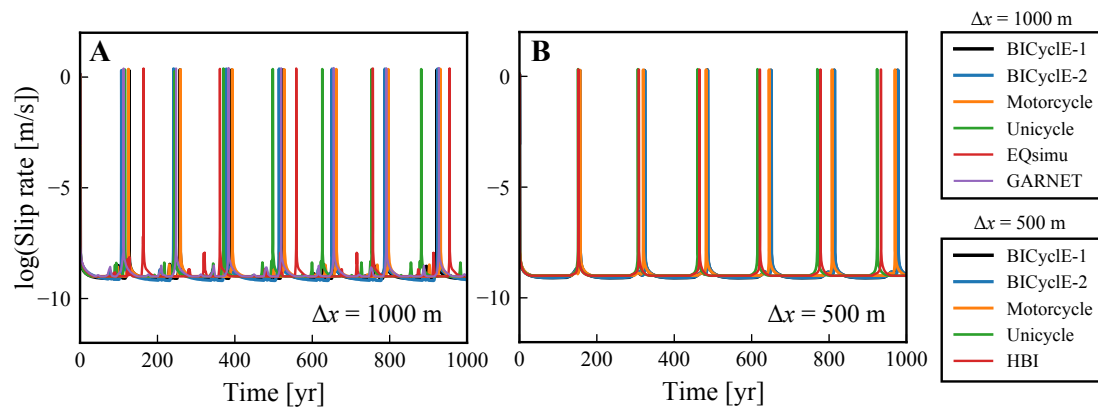
Figure 5. Time evolution of maximum slip rates in BP4-QD simulations. The time series of logarithmic maximum slip rates within the seismogenic zone are shown for simulations with (a) $\Delta x = 1000$ m and (b) $\Delta x = 500$ m. Logarithms with base 10 are shown in this and all later figures. Legend labels show code names in this and all later figures.
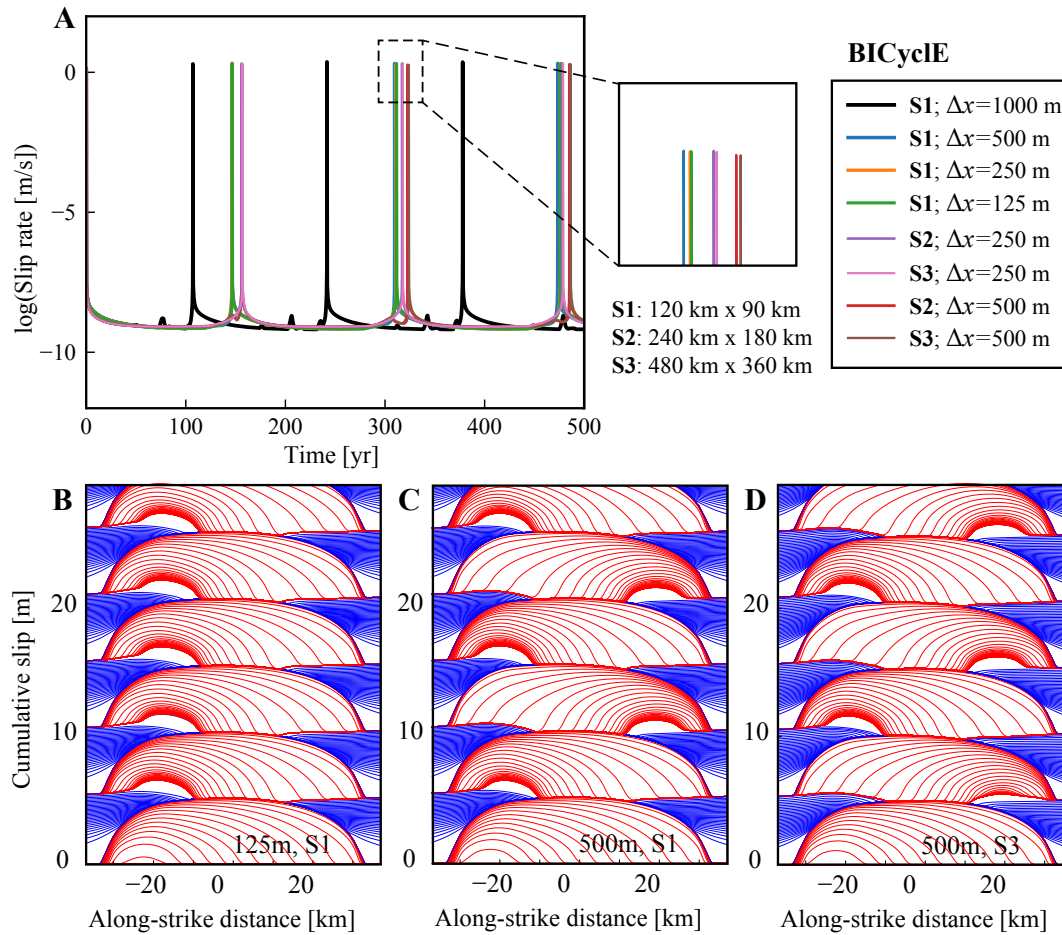
Figure 6. Effect of computational grid spacing and domain size on the self-convergence of SBEM simulations. (a) Time evolution of maximum slip rates for a suite of SBEM simulations with different grid spacings ($\Delta x = 125$, 250, 500, and 1000 m) and domain sizes: $(L_2, L_3) = (120\,\text{km}, 90\,\text{km})$, $(240\,\text{km}, 180\,\text{km})$, or $(480\,\text{km}, 360\,\text{km})$, denoted as S1, S2, or S3, respectively. Cumulative slip in the along-strike direction is plotted every 2 s for the seismic period (red lines) and every 5 yr for the aseismic period (blue lines) in three simulations with (b) $\Delta x = 125$ m and S1; (c) $\Delta x = 500$ m and S1; and (d) $\Delta x = 500$ m and S3.
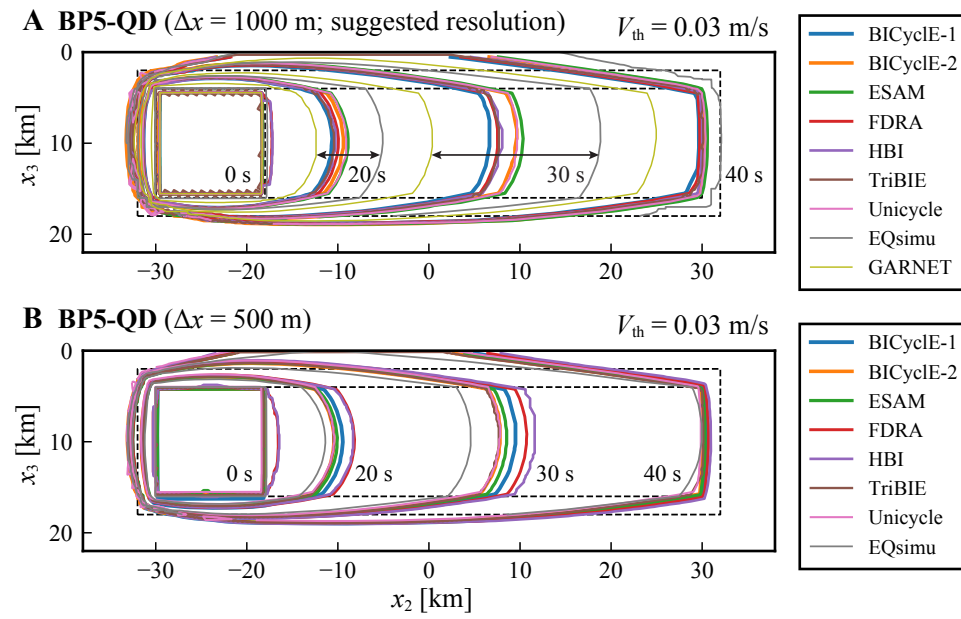
Figure 7. Rupture fronts of the first earthquake in BP5-QD simulations with different numerical resolutions. The contours of rupture fronts indicate 0, 20, 30, and 40 s after the earthquake initiation time in simulations with (a) $\Delta x = 1000$ m and (b) $\Delta x = 500$ m. The threshold slip rate for the coseismic phase, $V_{th} = 0.03$ m/s, is different from that in Figure 4.
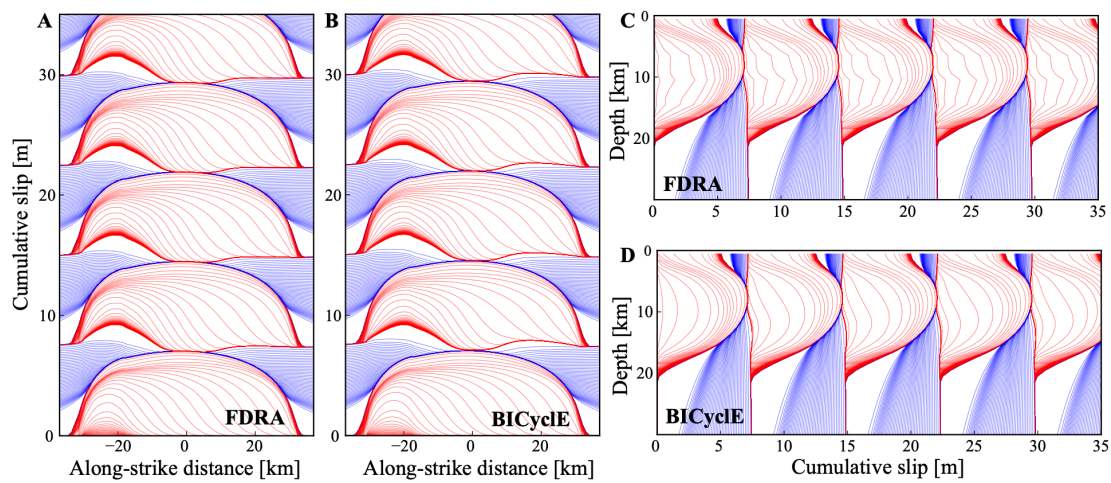
Figure 8. Fault slip evolution in selected BP5-QD simulations. Cumulative fault slip in two simulations ($\Delta x = 1000$ m) using FDRA and BICyclE are shown in the (a and b) along-strike and (c and d) along-depth directions. The seismic slip (red lines) is plotted every 2 s and aseismic slip (blues lines) is plotted every 5 yr. Note that downsampling and interpolation of simulation outputs in space and time sometimes affects visualization, such as panel c here.
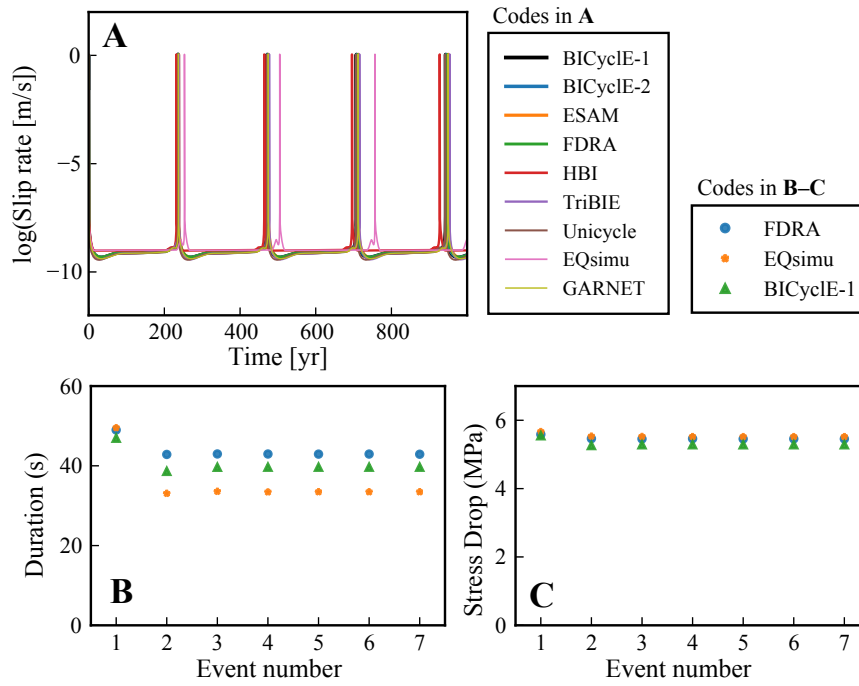
Figure 9. Long-term fault behavior and earthquake characteristics in BP5-QD simulations. (a) Time evolution of maximum slip rates in the seismogenic zone and (b) rupture duration and (c) stress drop for the first seven earthquakes are shown for simulations with $\Delta x = 1000$ m.
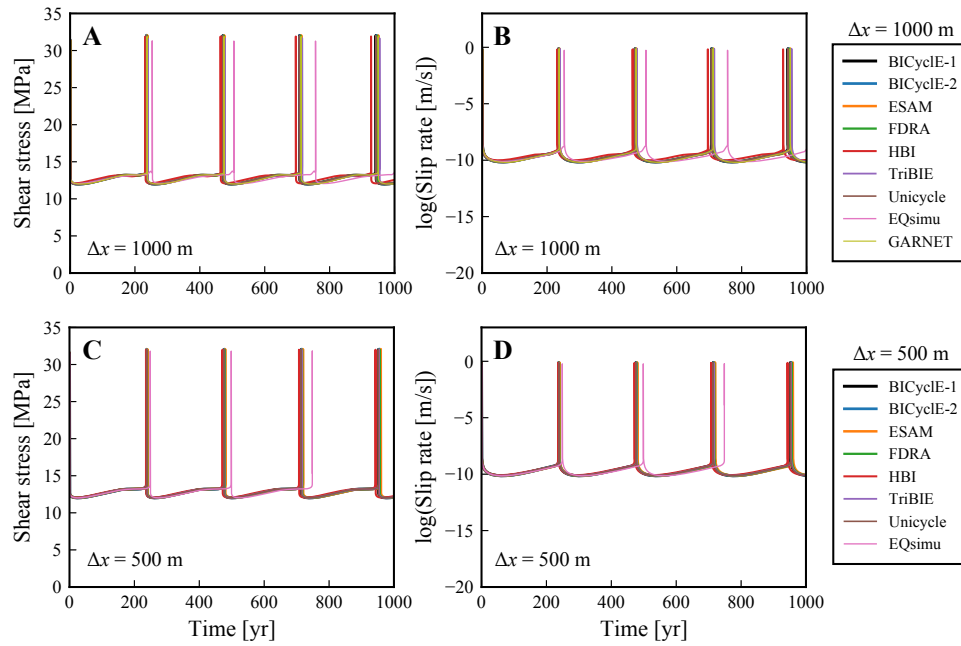
Figure 10. Long-term fault behavior at the surface in BP5-QD simulations. (a and c) Shear stress and (b and d) slip rates on the fault at the surface ($x_1 = x_2 = x_3 = 0$ km) in simulations with (a and b) $\Delta x = 1000$ m and (c and d) $\Delta x = 500$ m.
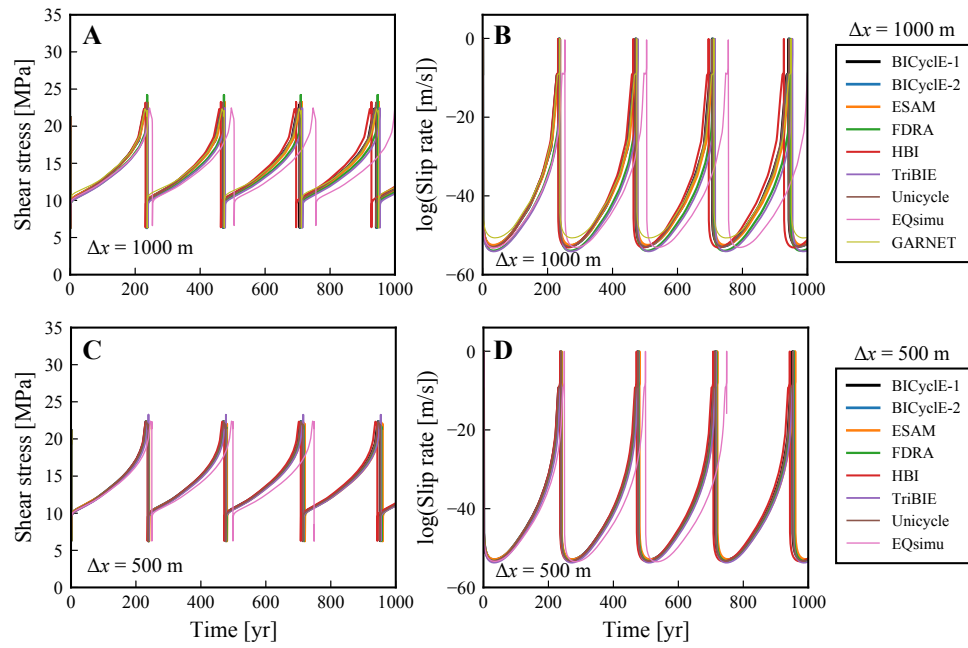
Figure 11. Long-term fault behavior at a seismogenic depth in BP5-QD simulations. (a and c) Shear stress and (b and d) slip rates on the fault at the mid-seismogenic depth ($x_1 = x_2 = 0\,\mathrm{km}; x_3 = 10\,\mathrm{km}$) in simulations with (a and b) $\Delta x = 1000\,\mathrm{m}$ and (c and d) $\Delta x = 500\,\mathrm{m}$.
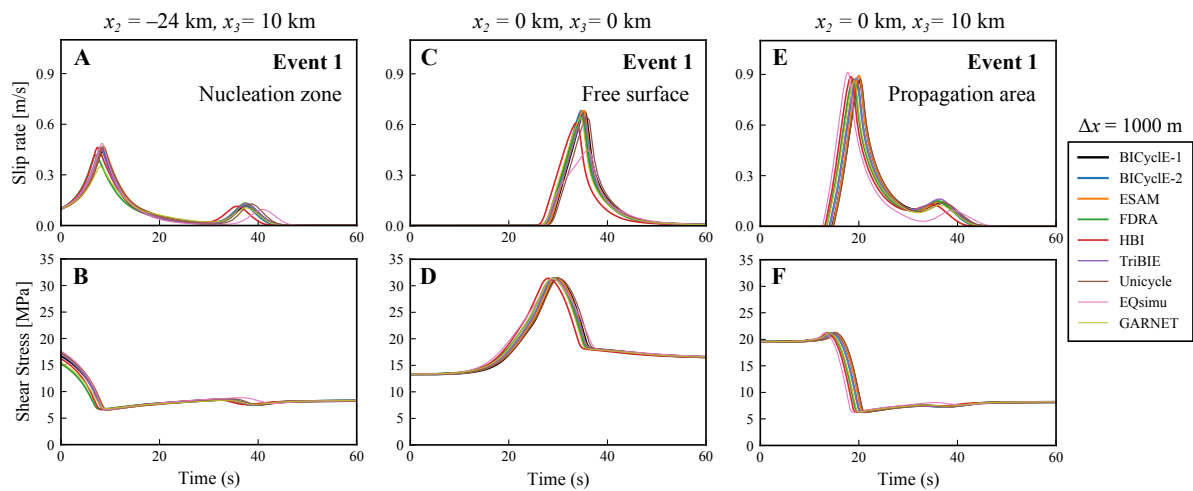
Figure 12. Coseismic rupture of the first event in BP5-QD simulations ($\Delta x = 1000$ m). Time evolution of (a, c, and e) slip rates and (b, d and f) shear stresses during the first earthquake are shown at different locations on the fault. Panels a and b refer to a point within the initial nucleation zone ($x_2 = -24$ km; $x_3 = 10$ km); c and d refer to a point at the free surface ($x_2 = 0$ km; $x_3 = 0$ km); e and f refer to a point within the propagation zone ($x_2 = 0$ km; $x_3 = 10$ km).
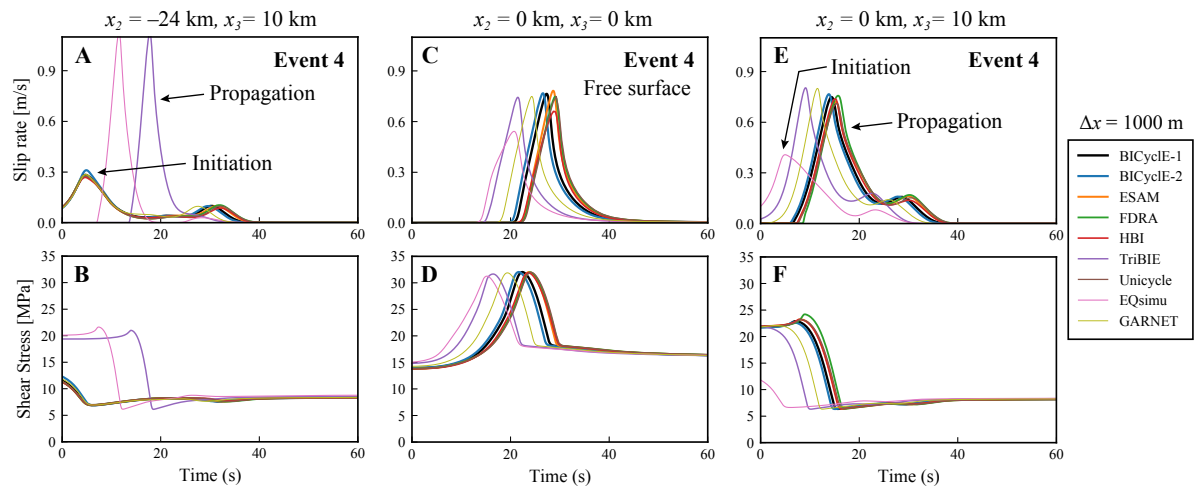
Figure 13. Coseismic rupture of the fourth event in BP5-QD simulations ($\Delta x = 1000$ m). Time evolution of (a, c, and e) coseismic slip rates and (b, d and f) shear stresses are shown at the same locations on the fault as in Figure 12.

Figure 14. Coseismic rupture of the sixth event in BP5-QD simulations (Δx = 500 and 250 m). Time evolution of (a, c, and e) coseismic slip rates and (b, d and f) shear stresses are shown at the same locations on the fault as in Figure 12.
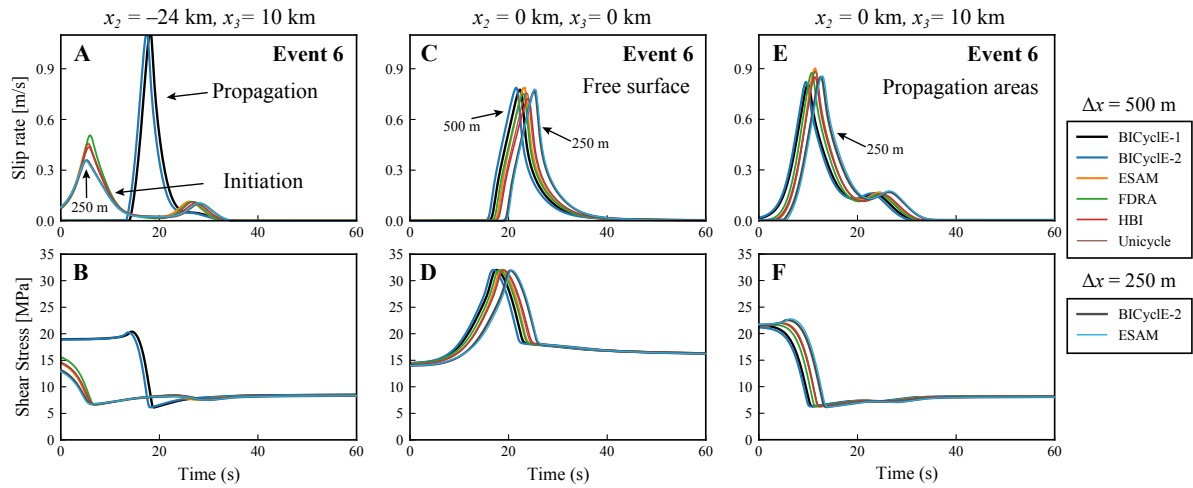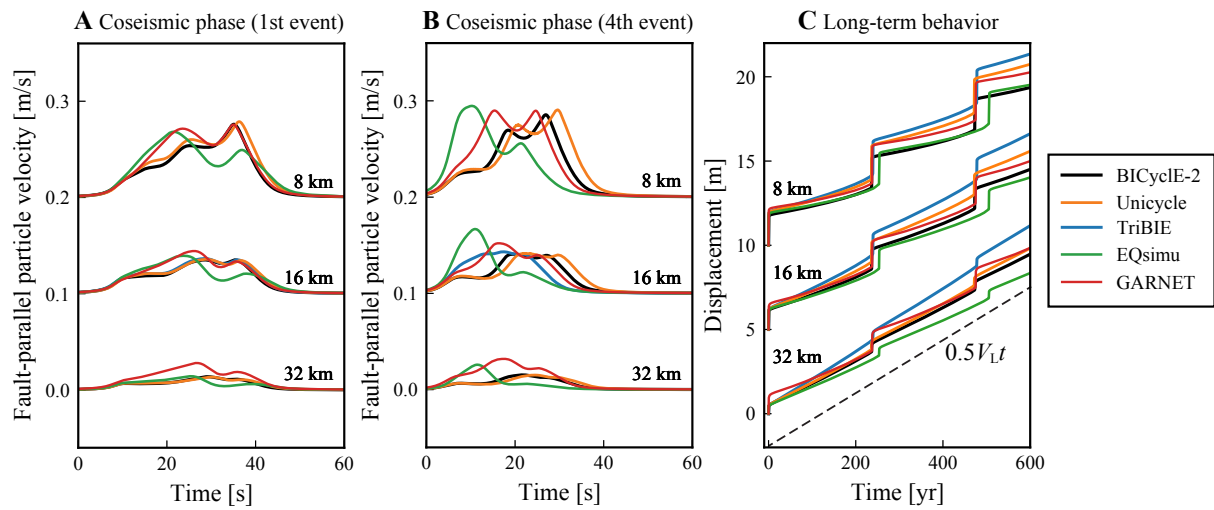
Figure 15. Off-fault ground movement in BP5-QD simulations. Fault-parallel displacement rates v_2 during the (a) first and (b) fourth events, and (c) long-term displacement history are shown at three off-fault locations on the surface ($x_1 = 8$, 16, or 32 km; $x_2 = 0$ km; $x_3 = 0$ km). The dashed line indicates the far-field surface displacement $0.5 V_L t$. The time series corresponding to different locations and the dashed line are vertically offset for visualization purpose.
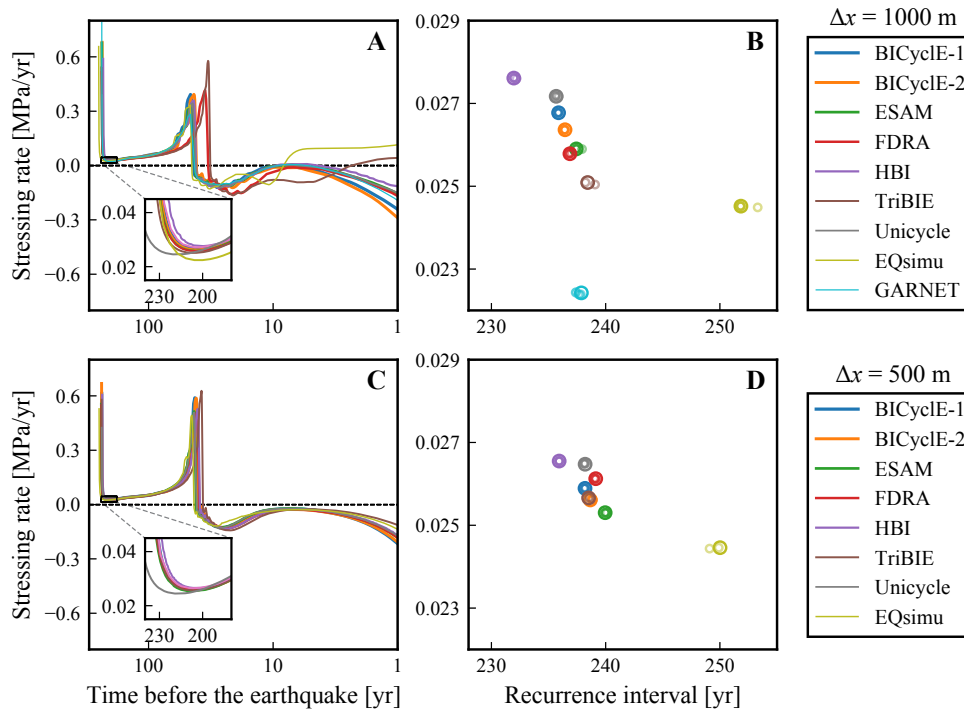
Figure 16. Interseismic stressing rate history and earthquake recurrence intervals in BP5-QD simulations. (a and c) Stressing rates at the mid-seismogenic depth ($x_2 = 0$ km; $x_3 = 10$ km) during the postseismic and interseismic periods before the sixth earthquake. (b and d) The minimum interseismic stressing rates (enlarged windows in a and c) and recurrence intervals are shown for the corresponding events (large circles in color) and preceding events (smaller circles in the same color). Simulations with $\Delta x = 1000$ m and $\Delta x = 500$ m are shown in panels a–b and c–d, respectively. Due to a shorter simulation time, the fourth event from TriBIE and EQsimu is considered in panels c–d.
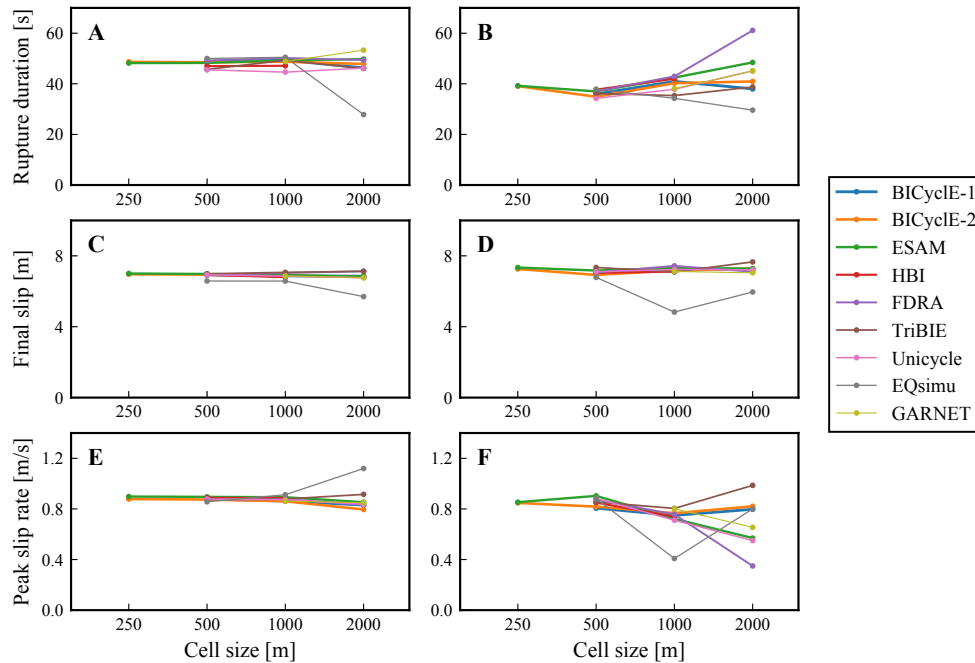
Figure 17. Comparison of earthquake characteristics in simulations with different resolutions. Coseismic rupture durations are shown for the (a) first and (b) sixth events in simulations with $\Delta x = 250, 500, 1000$, and 2000 m, when available. (c and d) Coseismic slip and (e and f) peak slip rate at the mid-seismogenic depth $(x_2 = 0 \, \text{km}; x_3 = 10 \, \text{km})$ are shown for the (c and e) first and (d and f) sixth event, respectively. Note an exception that the fourth event from TriBIE and EQsimu is considered for $\Delta x = 500 \, \text{m}$ in panels b, d, and f. Simulation results from each modeling group are plotted as line-connected dots.

Table 1.   Parameters in benchmark problems BP4-QD and BP5-QD

Parameter	Definition	Value in BP4	Value in BP5
ρ	density	$2670 \,\mathrm{kg/m^3}$	$2670 \,\mathrm{kg/m^3}$
c_s	shear wave speed	$3.464 \,\mathrm{km/s}$	$3.464 \,\mathrm{km/s}$
ν	Poisson's ratio	0.25	0.25
σ_n	effective normal stress on fault	$50 \,\mathrm{MPa}$	$25 \,\mathrm{MPa}$
L	characteristic state evolution distance	$0.008 \,\mathrm{m}$	$0.14 \,\mathrm{m}/0.13 \,\mathrm{m}^\dagger$
a_0	rate-and-state direct-effect parameter	0.0065	0.004
a_max	rate-and-state direct-effect parameter	0.025	0.04
b_0	rate-and-state evolution-effect parameter	0.013	0.03
V_L	plate loading rate	$10^{-9} \,\mathrm{m/s}$	$10^{-9} \,\mathrm{m/s}$
V_init	initial slip rate	$10^{-9} \,\mathrm{m/s}$	$10^{-9} \,\mathrm{m/s}$
V_i	elevated initial slip rate	$0.01 \,\mathrm{m/s}$	$0.03 \,\mathrm{m/s}$
V_0	reference slip rate	$10^{-6} \,\mathrm{m/s}$	$10^{-6} \,\mathrm{m/s}$
f_0	reference friction coefficient	0.6	0.6
H	(half-)width of uniform VW region	$15 \,\mathrm{km}$	$12 \,\mathrm{km}$
l	length of uniform VW region	$60 \,\mathrm{km}$	$60 \,\mathrm{km}$
$h(h_\mathrm{t})$	width of VW-VS transition zone	$3 \,\mathrm{km}$	$2 \,\mathrm{km}$
h_s	width of shallow VS zone	-	$2 \,\mathrm{km}$
W_f	(half-)width of rate-and-state fault	$40 \,\mathrm{km}$	$40 \,\mathrm{km}$
l_f	length of rate-and-state fault	-	$100 \,\mathrm{km}$
Δz	suggested grid spacing	$500 \,\mathrm{m}$	$1000 \,\mathrm{m}$
t_f	final simulation time	1500 years	1800 years
w	width of favorable nucleation zone	$12 \,\mathrm{km}$	$12 \,\mathrm{km}$
Λ_0	quasi-static process zone size	$2 \,\mathrm{km}$	$6 \,\mathrm{km}$
h^*	nucleation zone size	$12.4 \,\mathrm{km}$	$12.5 \,\mathrm{km}$

† The value used in the favorable nucleation zone.

Table 2.   Participating SEAS codes and modeling groups

Code Name	Type	Simulation† (Group Members)	BP4-QD	BP5-QD	Reference
BICyclE	SBEM	`jiang` (Jiang)	✓	✓	*Lapusta and Liu* (2009)
		`lambert` (Lambert, Lapusta)	✓	✓	
Motorcycle	SBEM	`barbot` (Barbot)	✓		*Barbot* (2021)
ESAM	BEM	`liu` (Y. Liu)		✓	*Liu and Rice* (2007)
FDRA	BEM	`cattania` (Cattania)		✓	*Segall and Bradley* (2012)
HBI	BEM	`ozawa` (Ozawa, Ando)	✓	✓	*Ozawa et al.* (2021)
TriBIE	BEM	`dli` (D. Li)		✓	*Li and Liu* (2016)
Unicycle	BEM	`barbot` (Barbot)	✓	✓	*Barbot* (2019)
EQsimu	FEM	`dliu` (D. Liu, Duan)	✓	✓	*Liu et al.* (2020)
GARNET	FDM	`li` (M. Li, Dal Zilio, Pranger, van Dinther)	✓	✓	*Pranger* (2020)

† The names of simulations displayed on our online platform

Table 3. Model parameters in BP4-QD simulations

Code Name	Simulation	Grid Spacing[a]	Domain Size[b]	BC[c]
BICyclE	`jiang`	1, 0.5	$(192, 96, \infty)$	P
	`lambert`	1, 0.5	$(180, 90, \infty)$	P
Motorcycle	`barbot`	1, 0.5	$(120, 80, \infty)$	P
HBI	`ozawa`	1, 0.5	$(120, 80, \infty)$	D
Unicycle	`barbot`	1, 0.5	$(120, 80, \infty)$	D
EQsimu	`dliu`	1	$(120, 120, 200)$	D
GARNET	`li`	1	$(120, 100, 120)$	D

[a] The grid spacings (in km) in simulations submitted by each modeling group.

[b] The total dimensions (in km) of the model domain in the format of (L_2, L_3, L_1).

[c] Displacement (D) or periodic (P) boundary conditions (BC) in the x_2/x_3 directions.

Table 4.   Model parameters in BP5-QD simulations

Code Name	Simulation	Grid Spacing[a]	Domain Size[a]	BC[a]
BICyclE	`jiang`	2, 1, 0.5	$(192, 96, \infty)$	P
	`lambert`	2, 1, 0.5, 0.25	$(180, 90, \infty)$	P
ESAM	`liu`	2, 1, 0.5, 0.25	$(128, 40, \infty)$	P/D[b]
FDRA	`cattania`	1, 0.5	$(10^4, 10^4, \infty)$	D
HBI	`ozawa`	1, 0.5	$(100, 40, \infty)$	D
TriBIE	`dli`	2, 1, 0.5	$(140, 60, \infty)$	D
Unicycle	`barbot`	2, 1, 0.5	$(100, 40, \infty)$	D
EQsimu	`dliu`	2, 1, 0.5	$(120, 60, 100)$	D
GARNET	`li`	2, 1	$(120, 60, 60)$	D

[a] Same parameters shown in Table 3.

[b] Periodic and displacement BCs in the along-strike and along-dip directions, respectively.

References

Abdelmeguid, M., X. Ma, and A. Elbanna (2019), A Novel Hybrid Finite Element-Spectral Boundary Integral Scheme for Modeling Earthquake Cycles: Application to Rate and State Faults With Low-Velocity Zones, *Journal of Geophysical Research: Solid Earth*, *124*(12), 12,854–12,881, doi:10/gkr74p.

Allison, K. L., and E. M. Dunham (2018), Earthquake cycle simulations with rate-and-state friction and power-law viscoelasticity, *Tectonophysics*, *733*, 232–256, doi:10.1016/j.tecto.2017.10.021.

Ampuero, J.-P., and A. M. Rubin (2008), Earthquake nucleation on rate and state faults – Aging and slip laws, *Journal of Geophysical Research: Solid Earth*, *113*(B1), doi:10.1029/ 2007JB005082.

Andrews, D. J. (1976a), Rupture propagation with finite stress in antiplane strain, *Journal of Geophysical Research (1896-1977)*, *81*(20), 3575–3582, doi:10/ddkswq.

Andrews, D. J. (1976b), Rupture velocity of plane strain shear cracks, *Journal of Geophysical Research (1896-1977)*, *81*(32), 5679–5687, doi:10/b2d43j.

Barall, M., and R. A. Harris (2014), Metrics for Comparing Dynamic Earthquake Rupture Simulations, *Seismological Research Letters*, *86*(1), 223–235, doi:10/gkr74z.

Barbot, S. (2018), Asthenosphere Flow Modulated by Megathrust Earthquake Cycles, *Geophysical Research Letters*, *45*(12), 6018–6031, doi:10/gdqdqs.

Barbot, S. (2019), Slow-slip, slow earthquakes, period-two cycles, full and partial ruptures, and deterministic chaos in a single asperity fault, *Tectonophysics*, p. 228171, doi:10/gf629v.

Barbot, S. (2021), A Spectral Boundary-Integral Method for Quasi-Dynamic Ruptures of Multiple Parallel Faults, *Bulletin of the Seismological Society of America*, *111*(3), 1614–1630, doi:10/ gkr75b.

Barbot, S., Y. Fialko, and Y. Bock (2009), Postseismic deformation due to the Mw 6.0 2004 Parkfield earthquake: Stress-driven creep on a fault with spatially variable rate-and-state friction parameters, *Journal of Geophysical Research: Solid Earth*, *114*(7), B07,405, doi:10.1029/ 2008JB005748.

Barbot, S., N. Lapusta, and J. P. Avouac (2012), Under the hood of the earthquake machine: Toward predictive modeling of the seismic cycle, *Science*, *336*(6082), 707–710, doi:10.1126/ science.1218796.

Bhat, H. S., R. Dmowska, G. C. P. King, Y. Klinger, and J. R. Rice (2007), Off-fault damage patterns due to supershear ruptures with application to the 2001 Mw 8.1 Kokoxili (Kunlun) Tibet earthquake, *Journal of Geophysical Research: Solid Earth*, *112*(6), 1–19, doi:10.1029/ 2006JB004425.

Buiter, S. J. H., G. Schreurs, M. Albertz, T. V. Gerya, B. Kaus, W. Landry, L. le Pourhiet, Y. Mishin, D. L. Egholm, M. Cooke, B. Maillot, C. Thieulot, T. Crook, D. May, P. Souloumiac,

and C. Beaumont (2016), Benchmarking numerical models of brittle thrust wedges, *Journal of Structural Geology*, *92*, 140–177, doi:10/f9bttc.

Cattania, C., and P. Segall (2019), Crack Models of Repeating Earthquakes Predict Observed Moment-Recurrence Scaling, *Journal of Geophysical Research: Solid Earth*, *124*(1), 476–503, doi:10.1029/2018JB016056.

Chen, T., and N. Lapusta (2009), Scaling of small repeating earthquakes explained by interaction of seismic and aseismic slip in a rate and state fault model, *Journal of Geophysical Research: Solid Earth*, *114*(1), B01,311, doi:10.1029/2008JB005749.

Dal Zilio, L., Y. van Dinther, T. V. Gerya, and C. C. Pranger (2018), Seismic behaviour of mountain belts controlled by plate convergence rate, *Earth and Planetary Science Letters*, *482*, 81–92, doi:10/gczxhs.

Day, S. M. (1982), Three-dimensional simulation of spontaneous rupture: The effect of nonuniform prestress, *Bulletin of the Seismological Society of America*, *72*(6), 1881–1902.

Day, S. M., L. A. Dalguer, N. Lapusta, and Y. Liu (2005), Comparison of finite difference and boundary integral solutions to three-dimensional spontaneous rupture, *Journal of Geophysical Research: Solid Earth*, *110*(B12), doi:10.1029/2005JB003813.

Dieterich, J. H. (1979), Modeling of rock friction 1. Experimental results and constitutive equations, *Journal of Geophysical Research, [Solid Earth]*, *84*(B5), 2161–2168, doi:10.1029/JB084iB05p02161.

Dieterich, J. H., K. B. Richards-Dinger, and K. A. Kroll (2015), Modeling Injection-Induced Seismicity with the Physics-Based Earthquake Simulator RSQSim, *Seismological Research Letters*, *86*(4), 1102–1109, doi:10/gg8hjn.

Duan, B., and S. M. Day (2008), Inelastic strain distribution and seismic radiation from rupture of a fault kink, *Journal of Geophysical Research: Solid Earth*, *113*(B12), doi:10/fthjcb.

Dublanchet, P. (2018), The dynamics of earthquake precursors controlled by effective friction, *Geophysical Journal International*, *212*(2), 853–871, doi:10/gcvdnw.

Dublanchet, P., P. Bernard, and P. Favreau (2013), Creep modulation of Omori law generated by a Coulomb stress perturbation in a 3-D rate-and-state asperity model, *Journal of Geophysical Research E: Planets*, *118*(9), 4774–4793, doi:10.1002/jgrb.50311.

Dunham, E. M., D. Belanger, L. Cong, and J. E. Kozdon (2011a), Earthquake Ruptures with Strongly Rate-Weakening Friction and Off-Fault Plasticity, Part 2: Nonplanar Faults, *Bulletin of the Seismological Society of America*, *101*(5), 2308–2322, doi:10/bnsr54.

Dunham, E. M., D. Belanger, L. Cong, and J. E. Kozdon (2011b), Earthquake Ruptures with Strongly Rate-Weakening Friction and Off-Fault Plasticity, Part 1: Planar Faults, *Bulletin of the Seismological Society of America*, *101*(5), 2296–2307, doi:10/d7t5n4.

Erickson, B. A., and E. M. Dunham (2014), An efficient numerical method for earthquake cycles in heterogeneous media: Alternating subbasin and surface-rupturing events on faults crossing a sedimentary basin, *Journal of Geophysical Research: Solid Earth*, *119*(4), 3290–3316, doi:10/gkr74x.

Erickson, B. A., E. M. Dunham, and A. Khosravifar (2017), A finite difference method for off-fault plasticity throughout the earthquake cycle, *Journal of the Mechanics and Physics of Solids*, *109*, 50–77, doi:10/gcg5ft.

Erickson, B. A., J. Jiang, M. Barall, N. Lapusta, E. M. Dunham, R. Harris, L. S. Abrahams, K. L. Allison, J.-P. Ampuero, S. Barbot, C. Cattania, A. Elbanna, Y. Fialko, B. Idini, J. E. Kozdon, V. Lambert, Y. Liu, Y. Luo, X. Ma, M. B. McKay, P. Segall, P. Shi, M. van den Ende, and M. Wei (2020), The Community Code Verification Exercise for Simulating Sequences of Earthquakes and Aseismic Slip (SEAS), *Seismological Research Letters*, *91*(2A), 874–890, doi:10.1785/0220190248.

Floyd, M. A., R. J. Walters, J. R. Elliott, G. J. Funning, J. L. Svarc, J. R. Murray, A. J. Hooper, Y. Larsen, P. Marinkovic, R. Bürgmann, I. A. Johanson, and T. J. Wright (2016), Spatial variations in fault friction related to lithology from rupture and afterslip of the 2014 South Napa, California, earthquake, *Geophysical Research Letters*, *43*(13), 6808–6816, doi:10/f82v2r.

Freund, L. (1998), *Dynamic Fracture Mechanics*, Cambridge Monographs on Mechanics, Cambridge University Press.

Gabriel, A. A., J. P. Ampuero, L. A. Dalguer, and P. M. Mai (2012), The transition of dynamic rupture styles in elastic media under velocity-weakening friction, *Journal of Geophysical Research, [Solid Earth]*, *117*(9), B09,311, doi:10.1029/2012JB009468.

Galis, M., C. Pelties, J. Kristek, P. Moczo, J.-P. Ampuero, and P. M. Mai (2015), On the initiation of sustained slip-weakening ruptures by localized stresses, *Geophysical Journal International*, *200*(2), 890–909, doi:10/f63pm9.

Goswami, A., and S. Barbot (2018), Slow-slip events in semi-brittle serpentinite fault zones, *Sci Rep*, *8*(1), 6181, doi:10/ggd8zm.

Harris, R. A., M. Barall, R. Archuleta, E. Dunham, B. Aagaard, J. P. Ampuero, H. Bhat, V. Cruz-Atienza, L. Dalguer, P. Dawson, S. Day, B. Duan, G. Ely, Y. Kaneko, Y. Kase, N. Lapusta, Y. Liu, S. Ma, D. Oglesby, K. Olsen, A. Pitarka, S. Song, and E. Templeton (2009), The SCEC/USGS Dynamic Earthquake Rupture Code Verification Exercise, *Seismological Research Letters*, *80*(1), 119–126, doi:10.1785/gssrl.80.1.119.

Harris, R. A., M. Barall, B. Aagaard, S. Ma, D. Roten, K. Olsen, B. Duan, D. Liu, B. Luo, K. Bai, J.-P. Ampuero, Y. Kaneko, A.-A. Gabriel, K. Duru, T. Ulrich, S. Wollherr, Z. Shi, E. Dunham, S. Bydlon, Z. Zhang, X. Chen, S. N. Somala, C. Pelties, J. Tago, V. M. Cruz-Atienza, J. Kozdon, E. Daub, K. Aslam, Y. Kase, K. Withers, and L. Dalguer (2018), A Suite of Exercises for Verifying Dynamic Earthquake Rupture Codes, *Seismological Research Letters*, *89*(3),

924   1146–1162, doi:10/gd3pzn.

925 Hori, T., N. Kato, K. Hirahara, T. Baba, and Y. Kaneda (2004), A numerical simulation of

926   earthquake cycles along the Nankai Trough in southwest Japan: Lateral variation in frictional

927   property due to the slab geometry controls the nucleation position, *Earth and planetary science*

928   *letters*, *228*(3), 215–226, doi:10.1016/j.epsl.2004.09.033.

929 Jiang, J., and Y. Fialko (2016), Reconciling seismicity and geodetic locking depths on the Anza

930   section of the San Jacinto fault, *Geophysical research letters*, *43*(20), 10,663–10,671, doi:10.

931   1002/2016GL071113.

932 Jiang, J., and N. Lapusta (2016), Deeper penetration of large earthquakes on seismically quiescent

933   faults, *Science*, *352*(6291), 1293–1297, doi:10.1126/science.aaf1496.

934 Jiang, J., and N. Lapusta (2017), Connecting depth limits of interseismic locking, microseismicity,

935   and large earthquakes in models of long-term fault slip, *Journal of Geophysical Research: Solid*

936   *Earth*, *122*(8), 6491–6523, doi:10.1002/2017JB014030.

937 Johnson, K. M., R. Bürgmann, and K. Larson (2006), Frictional properties on the San Andreas

938   fault near Parkfield, California, inferred from models of afterslip following the 2004 earthquake,

939   *Bulletin of the Seismological Society of America*, *96*(4 B), S321–S338, doi:10.1785/0120050808.

940 Kaneko, Y., J. P. Ampuero, and N. Lapusta (2011), Spectral-element simulations of long-term

941   fault slip: Effect of low-rigidity layers on earthquake-cycle dynamics, *Journal of Geophysical*

942   *Research, [Solid Earth]*, *116*(10), 1–18, doi:10.1029/2011JB008395.

943 Kato, N. (2016), Earthquake Cycles in a Model of Interacting Fault Patches: Complex Behavior

944   at Transition from Seismic to Aseismic Slip, *Bulletin of the Seismological Society of America*,

945   *106*(4), 1772–1787, doi:10/f8wkfz.

946 Kozdon, J. E., and E. M. Dunham (2013), Rupture to the Trench: Dynamic rupture simulations of

947   the 11 march 2011 Tohoku earthquake, *Bulletin of the Seismological Society of America*, *103*(2

948   B), 1275–1289, doi:10.1785/0120120136.

949 Lambert, V., and S. Barbot (2016), Contribution of viscoelastic flow in earthquake cycles within

950   the lithosphere-asthenosphere system, *Geophysical research letters*, *43*(19), 10,142–10,154,

951   doi:10.1002/2016GL070345.

952 Lapusta, N., and Y. Liu (2009), Three-dimensional boundary integral modeling of spontaneous

953   earthquake sequences and aseismic slip, *Journal of Geophysical Research, [Solid Earth]*, *114*(9),

954   doi:10.1029/2008JB005934.

955 Lapusta, N., and J. R. Rice (2003), Low-heat and low-stress fault operation in earthquake models of

956   statically strong but dynamically weak faults, *American Geophysical Union, Fall Meeting 2003,*

957   *abstract id. S51B-02*, p. B2.

958 Lapusta, N., J. R. Rice, Y. Ben-Zion, and G. Zheng (2000), Elastodynamic analysis for slow

959   tectonic loading with spontaneous rupture episodes on faults with rate- and state-dependent

friction, *Journal of Geophysical Research, [Solid Earth]*, *105*(B10), 23,765–23,789, doi:10.
1029/2000JB900250.

Li, D., and Y. Liu (2016), Spatiotemporal evolution of slow slip events in a nonplanar fault model
for northern Cascadia subduction zone, *Journal of Geophysical Research: Solid Earth*, *121*(9),
6828–6845, doi:10/f88d7f.

Li, D., and Y. Liu (2017), Modeling slow-slip segmentation in Cascadia subduction zone
constrained by tremor locations and gravity anomalies, *Journal of Geophysical Research: Solid
Earth*, *122*(4), 3138–3157, doi:10/f99bkr.

Liu, D., B. Duan, and B. Luo (2020), EQsimu: A 3-D finite element dynamic earthquake simulator
for multicycle dynamics of geometrically complex faults governed by rate- and state-dependent
friction, *Geophysical Journal International*, *220*(1), 598–609, doi:10/gj263v.

Liu, Y. (2013), Numerical simulations on megathrust rupture stabilized under strong dilatancy
strengthening in slow slip region, *Geophysical Research Letters*, *40*(7), 1311–1316, doi:10/
gkr74w.

Liu, Y., and J. R. Rice (2005), Aseismic slip transients emerge spontaneously in three-dimensional
rate and state modeling of subduction earthquake sequences, *Journal of Geophysical Research,
[Solid Earth]*, *110*(8), 1–14, doi:10.1029/2004JB003424.

Liu, Y., and J. R. Rice (2007), Spontaneous and triggered aseismic deformation transients in a
subduction fault model, *Journal of Geophysical Research, [Solid Earth]*, *112*(9), doi:10.1029/
2007JB004930.

Lozos, J. C., D. D. Oglesby, B. Duan, and S. G. Wesnousky (2011), The Effects of Double Fault
Bends on Rupture Propagation: A Geometrical Parameter Study, *Bulletin of the Seismological
Society of America*, *101*(1), 385–398, doi:10/bcr7j4.

Luo, B., B. Duan, and D. Liu (2020), 3D Finite-Element Modeling of Dynamic Rupture and
Aseismic Slip over Earthquake Cycles on Geometrically Complex Faults, *Bulletin of the
Seismological Society of America*, *110*(6), 2619–2637, doi:10/ghnnc7.

Luo, Y., J. P. Ampuero, P. Galvez, M. van den Ende, and B. Idini (2017), *QDYN: A Quasi-DYNamic
Earthquake Simulator (v1.1)*, doi:10.5281/zenodo.322459.

Ma, X., and A. Elbanna (2019), Dynamic rupture propagation on fault planes with explicit
representation of short branches, *Earth and Planetary Science Letters*, *523*, 115,702, doi:10/
gkr74m.

Marone, C. (1998), Laboratory-derived friction laws and their application to seismic faulting, *Annu.
Rev. Earth Planet. Sci.*, *26*(1), 643–696, doi:10/d9shmt.

Matsui, H., E. Heien, J. Aubert, J. M. Aurnou, M. Avery, B. Brown, B. A. Buffett, F. Busse, U. R.
Christensen, C. J. Davies, N. Featherstone, T. Gastine, G. A. Glatzmaier, D. Gubbins, J.-L.
Guermond, Y.-Y. Hayashi, R. Hollerbach, L. J. Hwang, A. Jackson, C. A. Jones, W. Jiang, L. H.

Kellogg, W. Kuang, M. Landeau, P. Marti, P. Olson, A. Ribeiro, Y. Sasaki, N. Schaeffer, R. D. Simitev, A. Sheyko, L. Silva, S. Stanley, F. Takahashi, S.-i. Takehiro, J. Wicht, and A. P. Willis (2016), Performance benchmarks for a next generation numerical dynamo model, *Geochemistry, Geophysics, Geosystems*, *17*(5), 1586–1607, doi:10/f8vkhm.

Maxwell, R. M., M. Putti, S. Meyerhoff, J.-O. Delfs, I. M. Ferguson, V. Ivanov, J. Kim, O. Kolditz, S. J. Kollet, M. Kumar, S. Lopez, J. Niu, C. Paniconi, Y.-J. Park, M. S. Phanikumar, C. Shen, E. A. Sudicky, and M. Sulis (2014), Surface-subsurface model intercomparison: A first set of benchmark results to diagnose integrated hydrology and feedbacks, *Water Resources Research*, *50*(2), 1531–1549, doi:10/f5zqnx.

McClure, M. W., and R. N. Horne (2011), Investigation of injection-induced seismicity using a coupled fluid flow and rate/state friction model, *GEOPHYSICS*, *76*(6), WC181–WC198, doi:10/fzj6qw.

Mckay, M. B., B. A. Erickson, and J. E. Kozdon (2019), A computational method for earthquake cycles within anisotropic media, *Geophysical Journal International*, *219*(2), 816–833, doi:10/gkr74j.

Mele Veedu, M., and S. Barbot (2016), The Parkfield tremors reveal slow and fast ruptures on the same asperity, *Nature*, *532*(7599), 361–365, doi:10/f8j8rw.

Michel, S., J.-P. Avouac, N. Lapusta, and J. Jiang (2017), Pulse-like partial ruptures and high-frequency radiation at creeping-locked transition during megathrust earthquakes, *Geophysical research letters*, *44*(16), 8345–8351, doi:10.1002/2017GL074725.

Mitsui, Y., and Y. Iio (2011), How did the 2011 off the Pacific coast of Tohoku Earthquake start and grow? the role of a conditionally stable area, *Earth, Planets and Space*, *63*(7), 755–759, doi:10.5047/eps.2011.05.007.

Nakata, R., M. Hyodo, and T. Hori (2012), Numerical simulation of afterslips and slow slip events that occurred in the same area in Hyuga-nada of southwest Japan: Simulation of afterslips and slow slip events, *Geophysical Journal International*, *190*(2), 1213–1220, doi:10/f344rw.

Nearing, G. S., B. L. Ruddell, M. P. Clark, B. Nijssen, and C. Peters-Lidard (2018), Benchmarking and Process Diagnostics of Land Models, *Journal of Hydrometeorology*, *19*(11), 1835–1852, doi:10/gfqkkr.

Nielsen, S. B., J. M. Carlson, and K. B. Olsen (2000), Influence of friction and fault geometry on earthquake rupture, *Journal of Geophysical Research: Solid Earth*, *105*(B3), 6069–6088, doi:10/c4z6zg.

Noda, H., M. Nakatani, and T. Hori (2013), A slower fault may produce a smaller preseismic moment rate: Non-1/tfacceleration of moment rate during nucleation and dependency on the background slip rate, *Geophysical research letters*, *40*(18), 4850–4854, doi:10.1002/grl.50962.

Okada, Y. (1992), Internal deformation due to shear and tensile faults in a half-space, *Bulletin of the Seismological Society of America*, *82*(2), 1018–1040.

Olsen, K. B., R. Madariaga, and R. J. Archuleta (1997), Three-Dimensional Dynamic Simulation of the 1992 Landers Earthquake, *Science*, *278*(5339), 834–838, doi:10/cwz9hp.

Ozawa, S., A. Ida, T. Hoshino, and R. Ando (2021), Large-scale earthquake sequence simulations of 3D geometrically complex faults using the boundary element method accelerated by lattice H-matrices on distributed memory computer systems, *arXiv:2110.12165*.

Palmer, A. C., and J. R. Rice (1973), The Growth of Slip Surfaces in the Progressive Failure of Over-Consolidated Clay, *Proceedings of the Royal Society A: Mathematical, Physical and Engineering Sciences*, *332*(1591), 527–548, doi:10.1098/rspa.1973.0040.

Perfettini, H., and J. P. Ampuero (2008), Dynamics of a velocity strengthening fault region: Implications for slow earthquakes and postseismic slip, *Journal of Geophysical Research, [Solid Earth]*, *113*(9), B09,411, doi:10.1029/2007JB005398.

Perfettini, H., and J. P. Avouac (2004), Stress transfer and strain rate variations during the seismic cycle, *Journal of Geophysical Research, [Solid Earth]*, *109*(6), doi:10.1029/2003JB002917.

Perfettini, H., and J. P. Avouac (2007), Modeling afterslip and aftershocks following the 1992 Landers earthquake, *Journal of Geophysical Research, [Solid Earth]*, *112*(7), B07,409, doi:10.1029/2006JB004399.

Pranger, C. C. (2020), Unstable physical processes operating on self-governing fault systems, Improved Modeling Methodology, Doctoral Thesis, ETH Zurich, doi:10.3929/ethz-b-000475293.

Qiu, Q., E. M. Hill, S. Barbot, J. Hubbard, W. Feng, E. O. Lindsey, L. Feng, K. Dai, S. V. Samsonov, and P. Tapponnier (2016), The mechanism of partial rupture of a locked megathrust: The role of fault morphology, *Geology*, *44*(10), 875–878, doi:10/f85mdp.

Rice, J. R. (1993), Spatio-temporal complexity of slip on a fault, *Journal of Geophysical Research: Solid Earth*, *98*(B6), 9885–9907, doi:10/c9gs59.

Rice, J. R., and S. T. Tse (1986), Dynamic motion of a single degree of freedom system following a rate and state dependent friction law, *Journal of Geophysical Research: Solid Earth*, *91*(B1), 521–530, doi:10/fgjzmm.

Richards-Dinger, K., and J. H. Dieterich (2012), RSQSim Earthquake Simulator, *Seismological Research Letters*, *83*(6), 983–990, doi:10.1785/0220120105.

Ripperger, J., J. P. Ampuero, P. M. Mai, and D. Giardini (2007), Earthquake source characteristics from dynamic rupture with constrained stochastic fault stress, *Journal of Geophysical Research, [Solid Earth]*, *112*(4), doi:10.1029/2006JB004515.

Rubin, A. M., and J. P. Ampuero (2005), Earthquake nucleation on (aging) rate and state faults, *Journal of Geophysical Research, [Solid Earth]*, *110*(11), 1–24, doi:10.1029/2005JB003686.

Ruina, A. (1983), Slip instability and state variable friction laws, *Journal of geophysical research*, *88*(B12), 10,359–10,370, doi:10.1029/JB088iB12p10359.

Sathiakumar, S., S. Barbot, and J. Hubbard (2020), Earthquake Cycles in Fault-Bend Folds, *Journal of Geophysical Research: Solid Earth*, *125*(8), e2019JB018,557, doi:10/gm4t7s.

Savage, J. C., and R. O. Burford (1973), Geodetic determination of relative plate motion in central California, *Journal of geophysical research*, *78*(5), 832–845, doi:10.1029/JB078i005p00832.

Segall, P., and A. M. Bradley (2012), The Role of Thermal Pressurization and Dilatancy in Controlling the Rate of Fault Slip, *Journal of Applied Mechanics*, *79*(3), 031,013, doi:10.1115/1. 4005896.

Shi, Q., S. Barbot, S. Wei, P. Tapponnier, T. Matsuzawa, and B. Shibazaki (2020), Structural control and system-level behavior of the seismic cycle at the Nankai Trough, *Earth, Planets and Space*, *72*(1), 27, doi:10/gm4t7p.

Shi, Z., and S. M. Day (2013), Rupture dynamics and ground motion from 3-D rough-fault simulations, *Journal of Geophysical Research, [Solid Earth]*, *118*(3), 1122–1141, doi:10.1002/ jgrb.50094.

Tal, Y., and B. H. Hager (2018), The Slip Behavior and Source Parameters for Spontaneous Slip Events on Rough Faults Subjected to Slow Tectonic Loading, *Journal of Geophysical Research, [Solid Earth]*, *123*(2), 1810–1823, doi:10.1002/2017JB014737.

Thakur, P., Y. Huang, and Y. Kaneko (2020), Effects of Low-Velocity Fault Damage Zones on Long-Term Earthquake Behaviors on Mature Strike-Slip Faults, *Journal of Geophysical Research: Solid Earth*, *125*(8), e2020JB019,587, doi:10/gm3rfn.

Tse, S. T., and J. R. Rice (1986), Crustal earthquake instability in relation to the depth variation of frictional slip properties, *Journal of geophysical research*, *91*(B9), 9452, doi:10.1029/ JB091iB09p09452.

Tullis, T. E., K. Richards-Dinger, M. Barall, J. H. Dieterich, E. H. Field, E. M. Heien, L. H. Kellogg, F. F. Pollitz, J. B. Rundle, M. K. Sachs, D. L. Turcotte, S. N. Ward, and M. B. Yikilmaz (2012), Generic Earthquake Simulator, *Seismological Research Letters*, *83*(6), 959–963, doi:10.1785/0220120093.

Tymofyeyeva, E., Y. Fialko, J. Jiang, X. Xu, D. Sandwell, R. Bilham, T. K. Rockwell, C. Blanton, F. Burkett, A. Gontz, and S. Moafipoor (2019), Slow slip event on the southern San Andreas fault triggered by the 2017 Mw 8.2 Chiapas (Mexico) earthquake, *Journal of Geophysical Research: Solid Earth*, *124*(9), 9956–9975, doi:10/gf5zsv.

Van Dinther, Y., T. V. Gerya, L. A. Dalguer, F. Corbi, F. Funiciello, and P. M. Mai (2013), The seismic cycle at subduction thrusts: 2. Dynamic implications of geodynamic simulations validated with laboratory models, *Journal of Geophysical Research, [Solid Earth]*, *118*(4), 1502–1525, doi:10.1029/2012JB009479.

1103 Wang, L., and S. Barbot (2020), Excitation of San Andreas tremors by thermal instabilities below

1104   the seismogenic zone, *Science Advances*, *6*(36), eabb2057, doi:10/gm4t7q.

1105 Wollherr, S., A.-A. Gabriel, and P. M. Mai (2019), Landers 1992 "Reloaded": Integrative Dynamic

1106   Earthquake Rupture Modeling, *J. Geophys. Res. Solid Earth*, *124*(7), 6666–6702, doi:10/gkr74c.

1107 Xu, J., H. Zhang, and X. Chen (2015), Rupture phase diagrams for a planar fault in 3-D full-space

1108   and half-space, *Geophys. J. Int.*, *202*(3), 2194–2206, doi:10/gkr74f.

1109 Zhu, W., K. L. Allison, E. M. Dunham, and Y. Yang (2020), Fault valving and pore pressure

1110   evolution in simulations of earthquake sequences and aseismic slip, *Nat Commun*, *11*(1), 4833,

1111   doi:10/gm4t7t.